The effect of the environment on the evolution of galaxy colours

Davies, Gregory Tudor

The Effect of the Environment on the Evolution of Galaxy Colours

MSc (One Volume)

Department of Physics, Durham University

Gregory Tudor Davies

May 31, 2006

Contents

1 Overview of Cosmology and Galaxy Formation **12**

1.1 Introduction to Modern Cosmology 12

1.1.1 The Big Bang 12

1.1.2 The Cosmic Microwave Background Radiation 13

1.1.3 Dark Matter and the Formation of Galaxies 15

1.1.4 Dark Energy 19

1.2 Galaxy Types and Star Formation Rates 20

1.2.1 The Galaxy Luminosity Function 20

1.2.2 The Hubble Sequence 21

1.2.3 Measuring Star Formation Rates in Galaxies 25

1.2.4 The Decline in SFR 27

1.2.5 Red and Blue Galaxies 33

1.3 Galaxy Photometry 36

1.3.1 Photometric Systems 36

1.3.2 The Johnson-Morgan-Cousins Photometric System 37

1.3.3 The SDSS Photometric System 38

1.3.4 The Kron Photometric System 40

1.3.5 The Petrosian Photometric System 42

1.3.6 K-Corrections 43

1.3.7 E-Corrections 45

2 Data **46**

2.1 Overview of Current High Redshift Surveys 46

2.1.1 The Deep Extragalactic Evolutionary Probe (DEEP) survey . . 46

2.1.2 The Gemini Deep Deep Survey (GDDS) 48

2.1.3 The Vimos VLT Deep Survey (VVDS) 49
2.1.4 The Great Observatories Origins Deep Survey (GOODS) 49
2.1.5 The zCOSMOS Survey 50
2.2 The DEEP1 (Groth Strip) Data 51
2.2.1 The Volume Limited Sample 51
2.2.2 K-Corrections to Groth Strip Data 53

3 Analysis **54**
3.1 Methods of Measuring Environmental Density 54
3.1.1 Cosmological Distances 54
3.1.2 Number of Counts in an Aperture 60
3.1.3 Voronoi Volume 61
3.2 Measuring Environmental Density in the Groth Strip Volume Limited Sample 62
3.2.1 Survey Edges 64
3.3 Fitting the Double Gaussians 66
3.4 The Ratio of Galaxies that are red 69
3.5 Colour Conversions between different Photometric Systems 69
3.6 Density Corrections 73

4 Results **74**
4.1 My Results 74
4.2 Comparison of the two Epochs 75
4.3 The Evolution of Galaxy Colours 76
4.4 What caused the Shift in the Mean Colour between z $\sim$ 1 and z $\sim$ 0? . 78

5 Discussion & Conclusions **82**

List of Figures

1.1 The WMAP image of the Cosmic Background Radiation [25] 14

1.2 The Cosmic Microwave Background Power Spectrum. [23] 15

1.3 This diagram shows that, on the largest angular scales, we are seeing the primordial fluctuations themselves. Time is increasing from left to right and, as it does so, the size of the universe at that time is shown schematically in the vertical size of the diagram. The two "horizon" lines denote the limits of space that is causally connected (i.e. photons have had time to reach one part from the other) at a given time. The two lines with arrows pointing towards the CMB observer (i.e. a present day astronomer) denote the angle at which the astronomer is looking at the CMB. Heuristically, one piece of matter only attracts another piece of matter gravitationally when the two pieces are within each other's horizon. The process of infall begins before the time of last scattering for regions that are causally connected at that epoch. However, it is only at the time of last scattering that the CMB photons become free to move towards the astronomer. Thus the horizon scale at this time becomes "frozen". We cannot see the Universe as it was before this time and no infall on scales larger than this will have begun by this time. Therefore, when we look at the CMB today at angular scales larger than the horizon at the last scattering surface, the anisotropies we see will not have resulted from the process of infall. They will be the remnants of the primordial fluctuations themselves. [45] 16

1.4 In contrast to 1.3, looking at smaller angular scales than the horizon scale at decoupling shows the process of structure formation at work [46] 17

1.5 Comparison of various estimates of the K-band luminosity. In both panels, the solid lines shows an estimate of the Ks luminosity function [17]. In the lower panel, the dotted line shows an estimate of the Schechter K-band luminosity function inferred from the SDSS z*-band luminosity function of [10]. 22

1.6 Galaxy types shown in the "Hubble Sequence". [24] 22

1.7 Integrated spectra of elliptical (top left panel), Sa (top right panel), Sc (bottom left panel) and an irregular galaxy (bottom right panel). The fluxes have been normalised to unity at 5500$\AA$. [52] 23

1.8 A schematic Hertzsprung-Russell diagram in which stars' luminosities are plotted against their temperatures. [48] 25

1.9 SFRD (from [50] derived from L([OII]) (circles) and from L(2,000$\AA$) (triangles). The diamonds are the values derived in [44]. The solid line is the fit derived in [17]. 28

1.10 The evolution of a gaseous disk of a spiral galaxy moving face on (left column) and inclined at 20^0 to the direction of motion (right column) through a diffuse, hot intra-cluster medium. The galaxy is moving at 2000kms^{-1} through an intra cluster medium (ICM) of density 2600 $h_{50}^{1/2}$ atoms m^{-3}. Each frame is 64kpc on one side. Perhaps surprisingly, 100% of the HI disk is lost within 100Myr. [66] 31

1.11 Simulations of a direct encounter (top) and a retrograde encounter (bottom) between two galaxies of equal mass. The grey scale shows logarithmic gas surface density. The contours show stellar surface density in steps of one magnitude. [5] 32

1.12 (From B04; SDSS galaxies). The distributions of u'-r' colours in luminosity and density bins. The distributions are again clearly bimodal . . 34

1.13 (From B04, SDSS galaxies). The mean colours of the red and blue distributions divided into their luminosity bins. 35

1.14 (From B04, SDSS galaxies). The fraction of galaxies that are red, as a function of density (left panel) and velocity dispersion (right panel), both divided into luminosity bins. 35

1.15 Transmission of the SDSS u', g', r', i', z' filters. The dotted curve is the quantum efficiency of a thinned UV-coated SITe CCD; this is the detector that is used in the definition of the SDSS system. [38]. 39

1.16 Kron radii R_1, as obtained from equation 1.30, are shown as a function of the radius R to which the integration was performed. Values of n range from 0.5, 1, 2, 3, ... 10. [40] 41

1.17 The logarithm of the Petrosian function $\eta(R)$ given by equation 1.34, shown as a function of normalised radius (R/R_e) for Sérsic profiles having n = 0.5, 1, 2, 3, ..., 10. [40] 43

1.18 Plot showing the typical SEDs (relative to the Johnson U and R filters) of an elliptical galaxy and a cD galaxy as seen at z=0 and at z=1. The fluxes have been normalised to those at $4000\mathring{A}$ in the rest frame in all 4 plots. Note: the SEDs in this figure are low resolution and do not show every spectral feature. They are those of Coleman, Wu and Weedman [18] 44

2.1 The Groth Strip Galaxies' right ascension vs. declination, colour coded according to the density of the local environment 51

2.2 Groth Strip galaxies M_B vs. z (magnitude limited sample). The dearth of fainter galaxies at higher redshifts renders the sample unusable for environment studies as it stands 52

3.1 Demonstration of Voronoi Volumes around galaxies [29] 61

3.2 Plot of the cube of the 5^{th} nearest neighbour distance versus vs the Voronoi volume. The galaxies plotted are only those that are not within 5 h^{-1} comoving Mpc of an edge of the survey. The strong agreement between the two is quantified by the Spearman ranked correlation coefficient of 0.85 62

3.3 The effects of redshift space distortion on each of the Voronoi method and the 3-dimensional n^{th} nearest neighbour method for n=3, 5. $\Delta_z(X)$ is defined in equation 3.28 and is plotted here for 5,031 galaxies in the DEEP2-selected simulation within $0.7 < z < 1.4$ and more than 4 h^{-1} comoving Mpc from any survey edge [29] 63

3.4 The Groth Strip Galaxies: histograms of (top left panel) the comoving radial separations (crs), (top right panel) the angular separations, (bottom left panel) the total separations, (bottom right panel) the galaxies' redshifts. The peak at the smallest angular separation is real but the peak at the smallest comoving radial separation is not. This peak is due to all crs that could have been inferred from a peculiar velocity of only 300 kms^{-1} being set to zero (see text). 65

3.5 Allowing for the edge effects. The distance to the 5^{th} nearest neighbour (r_5) of the galaxy whose density is being measured extends either side of the narrow survey area. The ellipse denotes the projection of a slice through the sphere of radius r_5. The volume of the sphere that is outside the survey must be removed before that volume can be used to calculate a density. 66

3.6 Histograms of the Groth Strip galaxies' U-B colours. Each histogram contains galaxies within a particular density range. The left most histogram contains the galaxies in the least dense environments, the right most contains galaxies in the most dense environments. The errors on the bars are simply the square roots of the bar heights. 70

3.7 The mean u'-r' colours of the red and blue distributions of galaxies from both the Groth Strip and from the SDSS. For comparative purposes, the conversion of the Groth Strip Galaxies' U-B colours into u'-r' was done via two sets of conversion tables, namely those of Fukugita et al [38] and of Krisciunas & Tonry [56]. Hence the two lines for each of the red and blue distributions of the Groth Strip galaxies 71

3.8 The fraction of red galaxies to the total number of galaxies as a function of environmental density for galaxies in the Groth Strip and for those in the SDSS 71

4.1 The evolution of galaxy u'-r' colours according to the PÉGASÉ software. Using the parameterisation defined in equation 4.1, A=1M⊙ (top left panel), 0.5M⊙ (top right panel), 0.01M⊙ (bottom left panel) and 0.0001M⊙ (bottom right panel). The red and blue horizontal lines show the mean colours from figure 3.7. The vertical black lines show the points in time at which the two sets of data in figure 3.7 are observed. Note that, since I am making the assumption that the galaxies formed at z=10 in this plot, these vertical black lines have been shifted left by the age of the universe at z=10. Thus, for a particular evolutionary track to be consistent with both sets of results for the blue galaxies, it must intersect the bottom left and top right hand corners of the rectangle formed by the two vertical black lines and the two horizontal blue lines and similarly for the red galaxies. It is clear that no track will provide an accurate match for either the red galaxies or the blue ones. 77

List of Tables

1.1 The names, central wavelengths and typical passbands of the filters used in the Johnson photometric system 38

1.2 The names, central wavelengths and typical passbands of the filters used in the SDSS photometric system. Note that the shape of the z' response function at long wavelengths is determined by the CCD sensitivity. . . 39

1.3 Theoretical Kron radii and magnitudes [40]. 42

2.1 Summary of the current high redshift galaxy spectroscopic surveys. Acronyms are as follows: DEEP - Deep Extragalactic Evolutionary Probe, GDDS - Gemini Deep Deep Survey, VVDS - Vimos VLT (Very Large Telescope) Deep Survey, GOODS - Great Observatories Origins Deep Survey, LRIS - Low Resolution Imaging Spectrograph, DEIMOS - DEep Imaging Multi Object Spectrograph, GMOS - Gemini Multi Object Spectrograph, CFHT - Canada France Hawaii Telescope, VIMOS - VIsible Multi Object Spectrograph, SST - Spitzer Space Telescope, HST - Hubble Space Telescope, XMM-N - X-ray Multi Mirror - Newton . . . 47

3.1 The values of n, χ^2 and the probability of getting at least that χ^2 given n for each of the 5 histograms in figure 3.6 68

4.1 The relative importance of density of environment, fraction of galaxies that are red and isolated evolution of galaxies in changing the average colour of galaxies from the z $\sim$ 1 epoch to z $\sim$ 0. The words high and low denote the high redshift and low redshift epochs whose values are assigned to each of the density, fraction and colour. For example, the third line down reveals that, when the fraction of galaxies that are red is set to the high redshift value but the density and colours of the red and blue distributions are left at the low redshift values, 12.0% of the shift in the mean colour between the epochs can be accounted for. . . . 80

Declaration

No material in this thesis has previously been submitted for a degree in this or any other university. The copyright of this thesis rests with the author. No quotation from it should be published in any format, including electronic and the Internet, without the author's prior consent. All information derived from this thesis must be acknowledged appropriately.

The Effect of the Environment on the Evolution of Galaxy Colours

by Gregory Tudor Davies, M.Sc. Thesis, May 2006

ABSTRACT

In chapter 1 of this thesis, I give a brief overview of the birth of modern cosmology and the growth of the current paradigm. I then go on to describe the different types of galaxies, the star formation rates within them and give some notes about galaxy photometry. In chapter 2 I give a brief overview of the current generation of high redshift galaxy surveys and describe the data, the analysis of which forms the original work in this thesis. This work is summarised below. In chapter 3 I describe the methods I used to carry out the work. I present my results in chapter 4 and my conclusions in chapter 5.

I present an analysis of the environmental dependence of the u'-r' colour distribution of 433 galaxies in a volume limited sample. The median redshift is 0.8. The sample was created from the Deep Extragalactic Evolutionary Probe 1 (DEEP) Groth Strip survey with magnitude and redshift limits given by $M_B \leq$ -19.0 and z $\leq$ 1.1 respectively. The environment was quantified using the spatial density of galaxies, measured in number Mpc^{-3}. Comparison of the results to those obtained by other authors from the Sloan Digital Sky Survey (SDSS) around z = 0.06 permits an analysis of the evolution of this colour distribution. The colour distributions from both surveys are well fitted by the sum of two Gaussian distributions, delineating two distinct galaxy populations. These are the early-types (red) and the late-types (blues). My first result is that the fraction of galaxies that are in the red population **increases** with environmental density. The proportion of galaxies that are red increases from 0.2 to 0.4 over 4 orders of magnitude of environmental density. That trend is much stronger at lower redshift. Further, the difference between the fractions of red galaxies in the two redshift regimes is **greatest** in the cluster environments. This difference is evidence of the Butcher-Oemler Effect. The mean colours of the two populations change **very little** as density increases. However, perhaps a very faint trend of the blue galaxies getting redder with increasing density is detected. Further analysis indicates that the change in galaxies' colours with cosmic time is almost entirely due to processes **intrinsic** to the galaxies themselves. Their environments make an almost negligible contribution to the colour change.

Chapter 1

Overview of Cosmology and Galaxy Formation

1.1 Introduction to Modern Cosmology

1.1.1 The Big Bang

The birth of modern cosmology can be traced to Edwin Hubble's ground breaking inference in 1929 that the universe is expanding. He had shown that "fuzzy nebulae", previously thought to have been part of our galaxy, were in fact other galaxies outside our own (e.g. [47]). Furthermore, using the relationships in 1.1, he deduced the recessional velocities of these other galaxies from their redshifts:

$$z = \frac{\lambda_o - \lambda_e}{\lambda_e} = \frac{v}{c} \tag{1.1}$$

where λ_e and λ_o are the wavelengths at which light from the galaxy in question is emitted and observed respectively.

Together with Milton Humason, Hubble formulated what is now known as Hubble's Law. This is an empirical velocity/distance relationship:

$$v = H_0 d \tag{1.2}$$

where H_0 is known as Hubble's constant. (It would later be shown that Hubble's constant was not in fact constant but that it decreases with cosmic time. It is now referred

to as Hubble's parameter). Hubble's Law, combined with the cosmological principle of a homogeneous and isotropic universe implied that the universe was expanding.

From an expanding universe, it was a short conceptual step to a big bang. If the universe was expanding, it must have been smaller in the past. So Big Bang theory, a central tenet of the Standard Model (and the crucial difference to the "Steady State" model), was born. Very briefly, in the Standard Model, astronomers believe that the Universe was born in a state of immense density, pressure and temperature. The exact nature of the universe at this time is beyond current physics. Albert Einstein's General Relativity theory predicts a gravitational singularity (where the curvature of spacetime is infinite) at this time. From this hot, dense state, the Universe expanded rapidly, according to the Standard Model, in a period of exponential inflation [42]. During this period of inflation, the universe became almost "flat". A flat universe is one that expands indefinitely but only asymptotically. This concept is explained more fully in 1.1.4.

1.1.2 The Cosmic Microwave Background Radiation

Some 300,000 years after the Big Bang, the temperature had cooled enough to allow electrons and protons to form neutral Hydrogen (they had previously formed a plasma). For this reason, this period is called the Period of Recombination. At the same time, however, the photons present at this early epoch became dissociated with the matter and the universe became transparent to radiation and this period is also called the Period of Decoupling or Time of last Scattering. Since the epoch of decoupling, the universe's expansion has redshifted those photons to microwave wavelengths. In 1948, George Gamow, Ralph Alpher and Robert Hernann predicted that these photons should still exist as a snapshot of the universe at this time. In 1965 Penzias & Wilson [64], having initially confused this remnant of the big bang with the dielectric properties of pigeon excrement, accidentally discovered the Cosmic Microwave Background (CMB) Radiation.

In 2004, the CMB was shown at unprecedented resolution by the Wilkinson Microwave Anisotropy Probe (WMAP). This map (shown in figure 1.1) of the CMB shows anisotropies in the temperature of relative size $\sim 10^{-5}$ on scales of tens of arcminutes

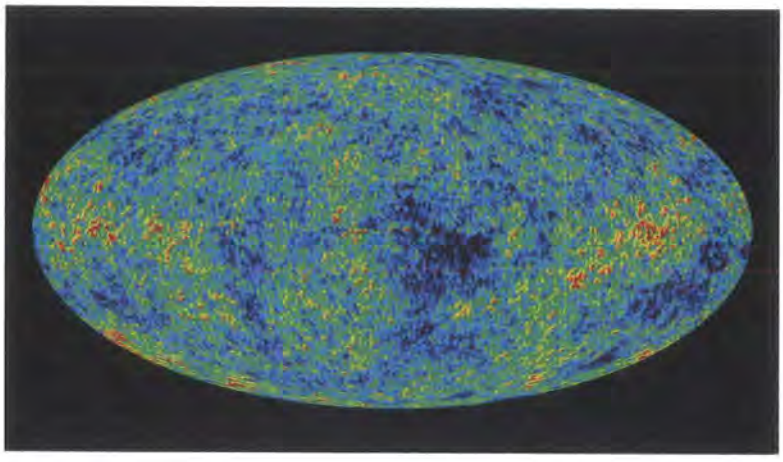

Figure 1.1: The WMAP image of the Cosmic Background Radiation [25]

to several degrees. The CMB is therefore not a perfect black body radiator. These anisotropies are believed to have arisen from quantum fluctuations around 10^{-37}s after the Big Bang (i.e. during the "Planck Time") that were expanded during inflation to form primordial fluctuations at decoupling. As described below, it is from these primordial fluctuations that today's galaxies and clusters of galaxies are believed to have formed.

When the baryons started to fall into the potential wells, regions of compressed and rarefied matter began to be enhanced. Gravity tries to compress the matter further and the internal pressure resists. Regions of compressed and rarefied air are what we know as sound and thus it may be helpful to consider an analogy with sound waves: there were "sound waves" in the early universe. The reason that we see, rather than hear, these "acoustic fluctuations" is that, when the gas is compressed, it heats up and vice versa. Thus the sound waves reveal themselves as the 1 in 100,000 temperature fluctuations on the sky that we see in the CMB.

Figure 1.2 shows the power spectrum of the CMB, as measured by WMAP. In other words, it is a plot of how strongly matter is clustered on different angular scales. The l numbers on the bottom of the x-axis of figure 1.2 are the multipole numbers which are related to the angular scale on the top of the x-axis by $\theta.l=180^0$. The l numbers are the subscripts from the spherical harmonics, solutions of Laplace's equation in spherical coordinates. i.e. as higher and higher integer numbers (l) of wavelengths are fitted around the sphere centred on the Earth, the plot of size of fluctuations on the scale of the angle subtended by the wavelength vs. l is the CMB power spectrum.

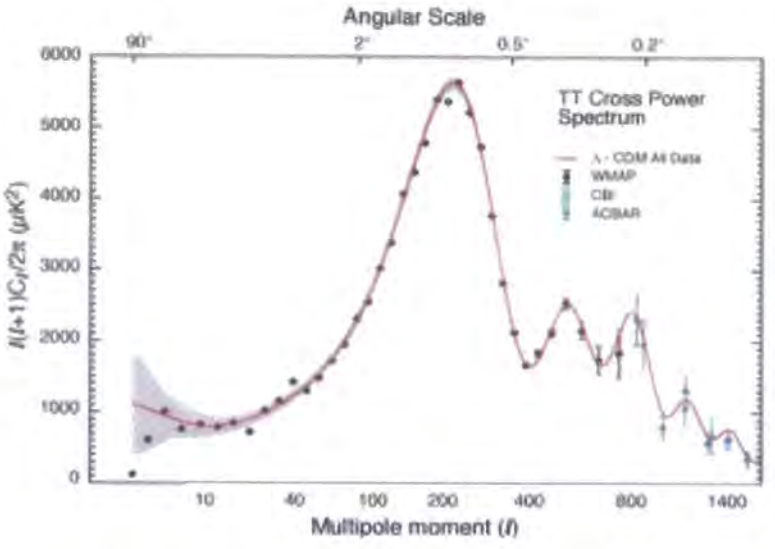

Figure 1.2: The Cosmic Microwave Background Power Spectrum. [23]

The peaks and troughs contain a lot of information about the origins of structure of the universe. For example, the position of the first peak gives the largest angular scale of parts of the sky that were in causal contact at decoupling. This idea is shown by figures 1.3 and 1.4. Thus, the power spectrum shows how matter is structured in the universe. When similar features were found in the 2 Degree Field Galaxy Redshift Survey (2dFGRS) power spectrum, it was confirmed that this picture of primordial fluctuations as gravitational instabilities producing the galaxies and clusters of galaxies of today is correct.

1.1.3 Dark Matter and the Formation of Galaxies

In 1933 Fritz Zwicky was observing the Coma Cluster. He noted that the galaxies at the edge of the cluster were orbiting at such high speeds that the amount of mass in the cluster, inferred from the cluster's brightness and number of galaxies, was about 400 times too small to provide the required centripetal force for the orbiting galaxies. He is credited with being the first person to invoke extra matter, in addition to what can be seen. Further powerful evidence comes from the rotation curves of galaxies (a plot of stars' orbital velocities versus their radial distance from the galactic centre). Simply equating a star's centripetal force to the gravitational attractive force it feels from its host galaxy of mass M yields:

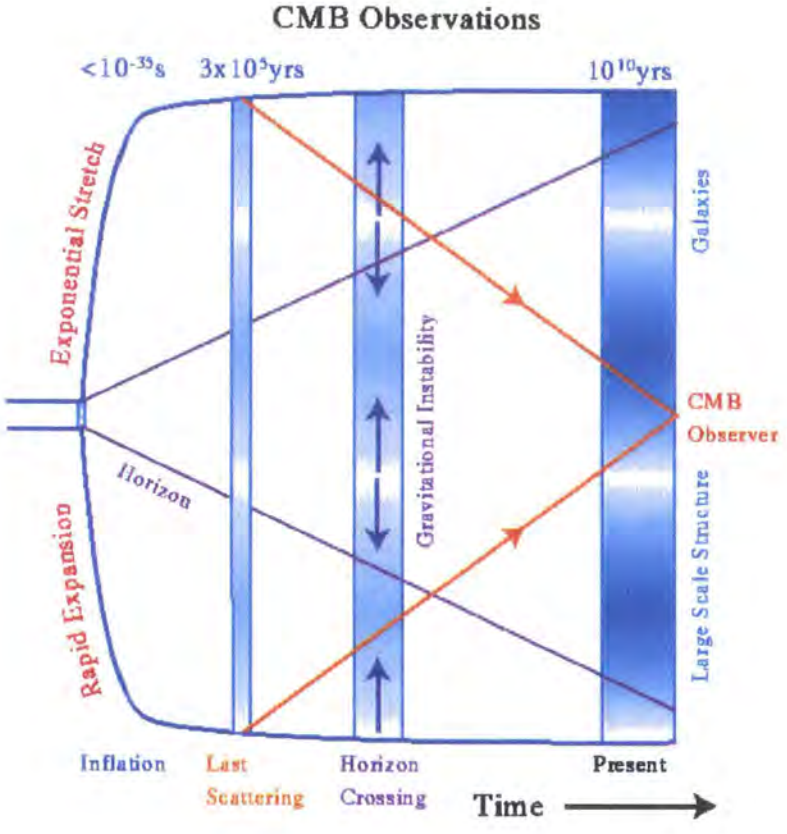

Figure 1.3: This diagram shows that, on the largest angular scales, we are seeing the primordial fluctuations themselves. Time is increasing from left to right and, as it does so, the size of the universe at that time is shown schematically in the vertical size of the diagram. The two "horizon" lines denote the limits of space that is causally connected (i.e. photons have had time to reach one part from the other) at a given time. The two lines with arrows pointing towards the CMB observer (i.e. a present day astronomer) denote the angle at which the astronomer is looking at the CMB. Heuristically, one piece of matter only attracts another piece of matter gravitationally when the two pieces are within each other's horizon. The process of infall begins before the time of last scattering for regions that are causally connected at that epoch. However, it is only at the time of last scattering that the CMB photons become free to move towards the astronomer. Thus the horizon scale at this time becomes "frozen". We cannot see the Universe as it was before this time and no infall on scales larger than this will have begun by this time. Therefore, when we look at the CMB today at angular scales larger than the horizon at the last scattering surface, the anisotropies we see will not have resulted from the process of infall. They will be the remnants of the primordial fluctuations themselves. [45]

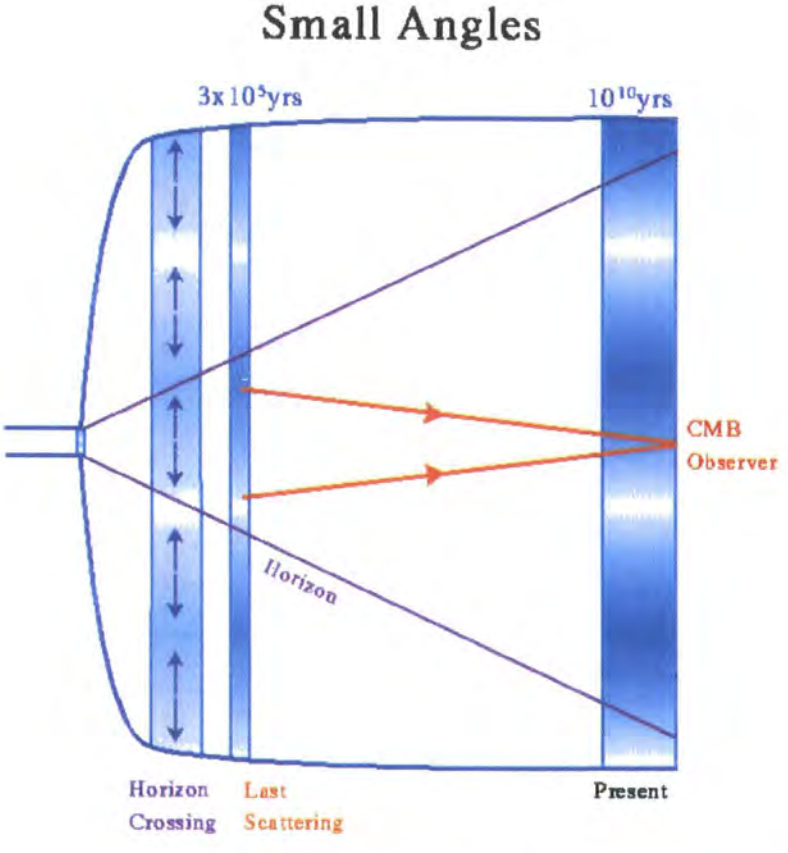

Figure 1.4: In contrast to 1.3, looking at smaller angular scales than the horizon scale at decoupling shows the process of structure formation at work [46]

$$\frac{mv^2}{r} = \frac{GMm}{r^2} \tag{1.3}$$

where m is the mass of the star, v is its orbital velocity, r is its radial distance from the galactic centre and G is the universal gravitational constant. If we assume that the amount of mass enclosed within a radius r of the centre is independent of radius, i.e.

$$M \neq M(r) \tag{1.4}$$

then further simplification leads to

$$v = \sqrt{\frac{GM}{r}} \tag{1.5}$$

However, the rotation curve is found to be flat. This means that v $\neq$ v(r) which necessitates

$$M(r) \propto r \tag{1.6}$$

A final piece of evidence for the existence of dark matter comes from the inferred merger histories and hierarchical structure formation of the present day galaxies. After decoupling, the primordial hydrogen and helium started clumping together and forming the first generation of stars. The clumping is due to the gravitational instabilities resulting from the primordial fluctuations in the power spectrum. The stars (along with other baryons simply in the forms of hot and cold gas) then clump together to form galaxies and later clusters of galaxies. However this bottom up approach requires the presence of cold dark matter. Ordinary baryonic matter had too high a temperature and too much pressure left over from the big bang to form the first stars by collapsing from the Jeans instability. The cold dark matter was required to provide the extra gravity to allow the initial collapse. It is believed that the gas out of which the stars would eventually form was initially mixed in with the dark matter. When the dark matter collapsed to form a halo, the gas cooled to form a disk and then more stars condensed out of the gas. This picture of the growth of structure in the universe is consistent with the distribution of galaxies in the present epoch, as shown by huge surveys such as the Sloan Digital Sky Survey (SDSS) and the 2DFGRS. Further, semi-analytic models (e.g. [16]) of galaxy formation incorporating this type of dark matter

have shown that the universe, as we see it, is consistent with this type of merging of structures using dark matter.

1.1.4 Dark Energy

There is one final twist to the story (at least in so far as the current paradigm is concerned). In the last few years (e.g. [70]), studies of Type Ia supernovae implied that the universe is not only expanding but is accelerating. This was a paradigm shift since it had previously been thought that the gravitational attraction of all matter in the universe must be slowing the expansion down, although it may not have been enough to stop it. The fact that the universe is accelerating means there must be something that is causing this acceleration. This strange new phenomenon has been termed "dark energy" because it cannot be seen and there is no evidence that it is matter based. In fact, it is very unlikely to be some form of matter because all known matter has attractive gravity. Dark energy must have some kind of "negative pressure" p related to its density ρ by w (which must be negative) in its equation of state:

$$w = p/\rho \tag{1.7}$$

The story of dark energy, however, goes back long before the current millennium. Consider Friedmann's equation that relates the Hubble parameter H, the scale factor (also known as the expansion parameter) of the universe a, the universal gravitational constant G, the density of the universe ρ, the dark energy Λ and the geometry of the universe quantified by k:

$$H^2 = \left(\frac{\dot{a}}{a}\right)^2 = \frac{8\pi G}{3}\rho + \frac{\Lambda}{3} - \frac{k}{a^2} \tag{1.8}$$

The Λ term is equivalent to Einstein's Cosmological Constant. His General Relativity equations had predicted that the universe would expand. Unable to reconcile this with his intuition, Einstein inserted this constant, representing a force that would oppose gravity, in order to keep the universe static. On hearing of Hubble's finding of an expanding universe, Einstein called the inclusion of this constant his greatest blunder. However, in the light of the type Ia supernovae results, this constant is again being seriously considered. Equation 1.8 can be simplified by re-parameterising in terms of

the critical density ρ_c. This is the density required to make the universe expand forever but only asymptotically. In other words the universe is flat and there is no dark energy. This corresponds to setting k = Λ = 0 into equation 1.8 yielding

$$\rho_c = \frac{3H^2}{8\pi G} \tag{1.9}$$

Then defining $\Omega_M = \rho_0/\rho_c$ and $\Omega_\Lambda = \Lambda/3H_0^2$, where the 0 subscript denotes present day values, equation 1.8 becomes

$$\Omega_M + \Omega_\Lambda - k = 1 \tag{1.10}$$

This means that, if the universe is flat (i.e. k=0) then all the energy in the universe is either matter (comprising both baryonic matter and dark matter) or dark energy. This is indeed the current paradigm, often labelled ΛCDM (Cold Dark Matter). It is the one that I shall be assuming throughout this work. More specifically, I shall be using the values (H_0, Ω_M, Ω_Λ, k) = (70, 0.3, 0.7, 0) where H_0 has been measured in $kms^{-1}Mpc^{-1}$. The value of Ω_M of 0.3 approximately comprises 0.05 (baryons) + 0.25 (dark matter). Thus, although it is only believed to dominate proceedings on the largest scales, dark energy comprises 70% of the universe's energy.

1.2 Galaxy Types and Star Formation Rates

1.2.1 The Galaxy Luminosity Function

I begin this section with a brief description of the galaxy luminosity function, i.e. the distribution of galaxies within a fixed volume of space in terms of their luminosity, (and the evolution thereof) is another property of the universe that any model of galaxy evolution must satisfy. In this sense, the luminosity function of galaxies in the current epoch is another piece of circumstantial evidence supporting the ΛCDM model described above. The most commonly used parameterisation of the galaxy luminosity function is that of the Schechter Luminosity Function. The Schechter parameterisation assumes that there are many more faint galaxies than there are bright ones and that, at the high luminosity end, the number diminishes rapidly with increasing luminosity.

In the Schechter parameterisation, α gives the slope of the faint end of the distribution, L_* gives a "characteristic luminosity" above which the number diminishes rapidly and n_* is a normalisation constant for the number ϕ of galaxies per unit volume per unit luminosity:

$$\phi(L)dL = n_*\left(\frac{L}{L_*}\right)^{\alpha} e^{-L/L_*}\frac{dL}{L_*} \tag{1.11}$$

Equation 1.11 can be re-parameterised using absolute magnitudes (M) instead of luminosities:

$$\phi(M)dM = \frac{2}{5}\phi^* ln10[10^{\frac{2}{5}(M^*-M)}]^{\alpha+1} e^{-10^{\frac{2}{5}(M^*-M)}}dM \tag{1.12}$$

Figure 1.5 shows a comparison of various estimates of the K-band luminosity function. The K-band luminosity is useful for two reasons. Firstly, the K-band falls in a window of atmospheric transmission and thus is suitable for observations from the ground. Secondly, for all but the highest redshift galaxies ($z < 4.5$), the $4000\mathring{A}$ break is below the 2.2micron wavelength where the K-band is centred. This is particularly useful when comparing real and mock luminosity functions because galaxy spectra are much easier to predict in this wavelength range so a disparity here would immediately signify a fundamental problem with the model. In both panels of figure 1.5, the solid lines shows an estimate of the Ks luminosity function [17]. In the lower panel, the dotted line shows an estimate of the Schechter K-band luminosity function inferred from the SDSS z*-band luminosity function of [10].

1.2.2 The Hubble Sequence

Figure 1.6 shows the major galaxy morphologies in Hubble's classic "tuning fork" diagram. Originally, Hubble thought that all galaxies evolved from left to right along this diagram (i.e. from early-type to late-type). This is no longer believed to be the whole story but, as will become apparent, the issue of galaxies transforming from one morphology to another is still a very pertinent one. The "E0" galaxies, as depicted on the extreme left of figure 1.6, are commonly known as elliptical or early-type galaxies. They are usually older than spiral galaxies, typically contain older stars, are not

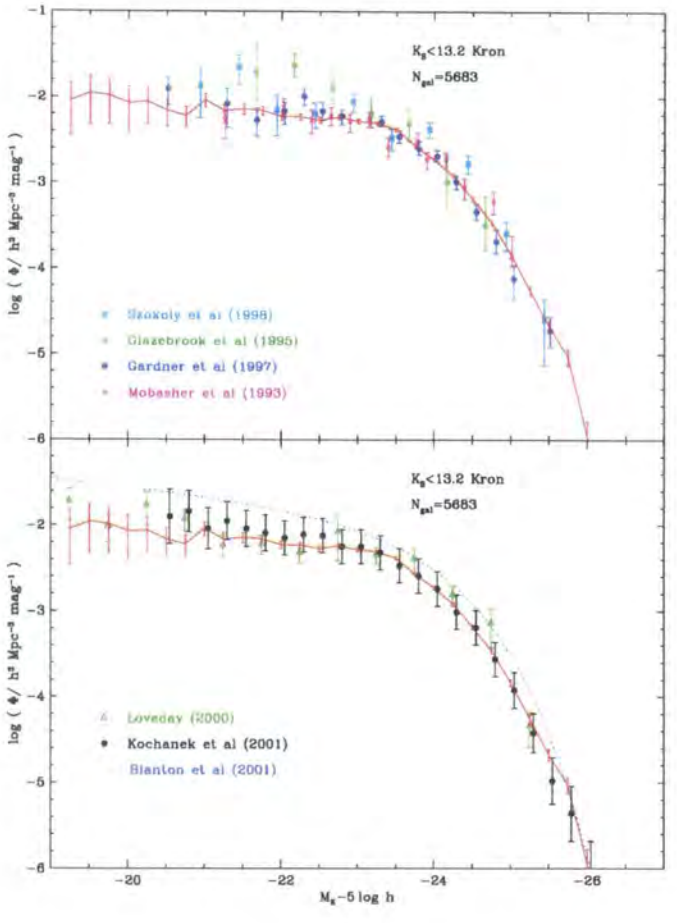

Figure 1.5: Comparison of various estimates of the K-band luminosity. In both panels, the solid lines shows an estimate of the Ks luminosity function [17]. In the lower panel, the dotted line shows an estimate of the Schechter K-band luminosity function inferred from the SDSS z*-band luminosity function of [10].

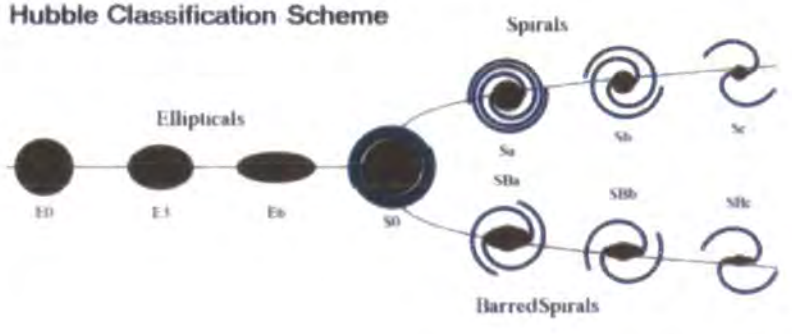

Figure 1.6: Galaxy types shown in the "Hubble Sequence". [24]

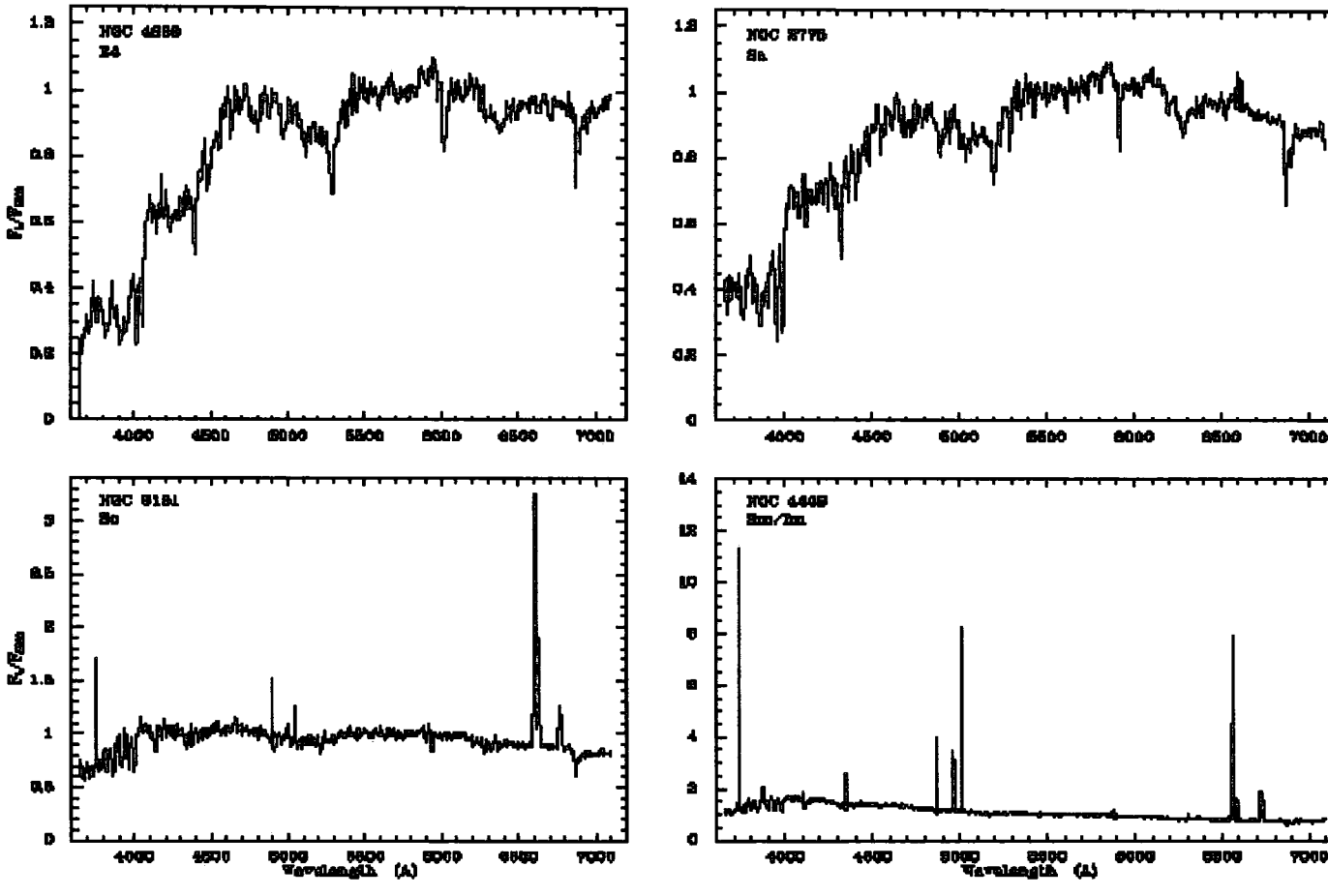

Figure 1.7: Integrated spectra of elliptical (top left panel), Sa (top right panel), Sc (bottom left panel) and an irregular galaxy (bottom right panel). The fluxes have been normalised to unity at 5500$\AA$. [52]

producing new stars and typically have a large bulge. (The term "early-type" is thus somewhat paradoxical since they tend to contain "late-type" stars). The spirals (barred and unbarred) shown on the right of figure 1.6 tend to be younger galaxies with active star forming regions and are labelled late-type galaxies and have more of a disk shape than a bulge. They tend to be bluer in colour whilst the ellipticals tend to be redder. The S0 galaxies, or lenticulars, are an example of an intermediate class between the two extremes of the Hubble Sequence.

How do the stellar populations of the different types of galaxies differ? Figure 1.7 shows the typical rest frame spectra of an elliptical galaxy (top left panel), an Sa type galaxy (top right panel), an Sc type galaxy (bottom left panel) and an irregular galaxy (bottom right panel). The spectra are normalised to unity at 5,500$\AA$. It is helpful to divide stars into two broad categories to explain the shape of these spectra, namely those on the main sequence (MS) of a Hertzsprung-Russell diagram (e.g. figure 1.8) and those that have moved off the main sequence to become red giants, super giants, etc. During stars' hydrogen-burning phase, they move up the MS (small vertical movement in figure 1.8). Thus, they are getting hotter (bluer). Thereafter, they move towards the top left of the HR diagram. i.e. they are getting cooler (redder) but larger and more luminous. Since this is a typical stellar evolutionary track, the red giants will be older than the bluer, hotter MS stars more often than not. However, it must be remembered that more massive stars evolve more quickly and so there will be some red giants that are younger than some of the MS stars.

A natural break in galaxies' spectra is formed at 4000$\AA$ because, shortward of this wavelength, stellar photospheric opacity is markedly increased. This is not only due to Ca II Fraunhofer H and K lines but also to a variety of elements heavier than helium in various stages of ionisation (e.g. [43]). The size of this break correlates with, among other things, stellar temperature. The elliptical galaxy has barely any flux at wavelengths shorter than 4,000$\AA$ indicating that its stars are older and cooler. Also, there is a distinct lack of emission lines which, as described below, shows that the galaxy is not producing any new stars. The size of the 4,000$\AA$ break is much smaller in the Sc galaxy because it has a population of young, hotter stars such that the fluxes either side of the break are comparable. There are also strong Hα (6562.8$\AA$) and [OII] (3727$\AA$) emission lines denoting active star formation. The irregular galaxy also has

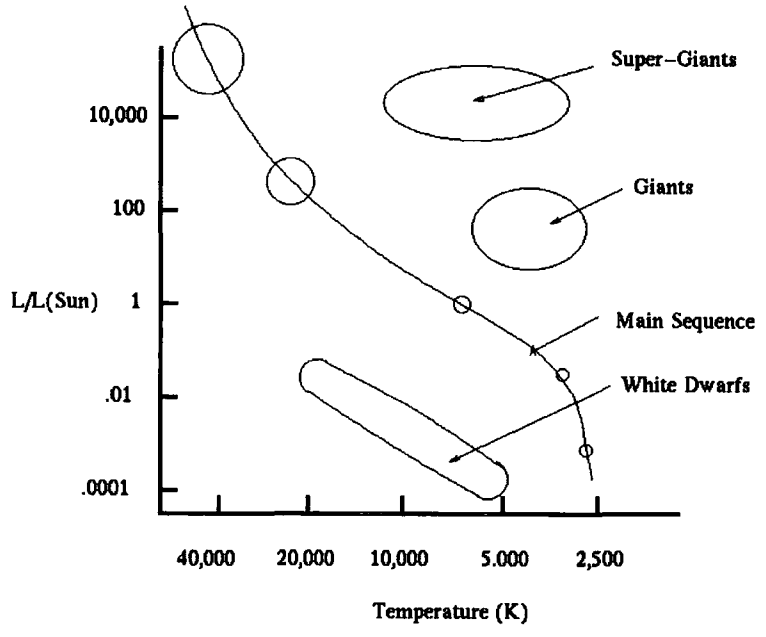

Figure 1.8: A schematic Hertzsprung-Russell diagram in which stars' luminosities are plotted against their temperatures. [48]

strong star formation and arguably less flux from its older stars than it does from its younger ones.

In fact, galaxies' star formation rates (SFR) are found to vary over a very large range. The SFR can be virtually zero in gas-poor ellipticals, S0s and dwarf galaxies. Gas-rich spirals may have $\sim 20 M_{\odot} yr^{-1}$, starburst galaxies up to $\sim 100 M_{\odot} yr^{-1}$. Even higher rates, up to $1{,}000 M_{\odot} yr^{-1}$ can be found in the most luminous IR starburst galaxies and are almost exclusively the preserve of galaxies undergoing tidal interactions and mergers. These are described further in section 1.2.4.

1.2.3 Measuring Star Formation Rates in Galaxies

How is the SFR, for example in units of $M_{\odot} Myr^{-1}$, of a galaxy inferred? When new stars form in a galaxy, they are embedded in a sea of neutral Hydrogen (an HI region). The massive, hot stars (O, B types) will emit flux over a wide range of wavelengths but some of it will be at wavelengths shorter than the Lyman limit for H. This is the energy required to remove an electron from the ground state (n=1) of neutral hydrogen to the $n=\infty$ state, i.e. to ionise the atom. Thus flux that is of a wavelength shorter than the Lyman limit ionises this sea of hydrogen on its way out of the galaxy (e.g. [51]).

As electrons then recombine with the hydrogen ions, they emit radiation at various wavelengths depending on the transition the electron undertakes during recombination. The lines produced by this process are called recombination lines and they effectively re-emit the galaxy's integrated stellar luminosity shortward of the Lyman limit, thus providing a direct, sensitive probe of the young, high mass stellar population. The H_α (or $Balmer_\alpha$, n=3 to n=2) line is the most commonly used recombination line. The wavelength of the transition between levels n_1 and n_2 in neutral hydrogen can be calculated using the Rydberg Formula:

$$\frac{1}{\lambda} = R_H\left(\frac{1}{n_1^2} - \frac{1}{n_2^2}\right) \tag{1.13}$$

where $R_H = 1.097 \times 10^{-7}$ m^{-1} and is known as the Rydberg constant.

Further, since these lines result almost exclusively from the flux from massive (> 19 $M_\odot$) and short lived ($\lesssim 20$ Myr) stars, the equivalent widths of these lines provide a near instantaneous measure of the SFR, independent of the SFR history. The calibration of the H_α luminosity as a measure of SFR depends on the initial mass function (IMF) and metallicity assumed. [52] quote the following, assuming a Salpeter IMF with mass limits 0.1 and 100 $M_\odot$ and solar abundances:

$$SFR(M_\odot yr^{-1}) = 7.9 \times 10^{-42} L(H\alpha)(ergs^{-1}) \tag{1.14}$$

where the H_α calibration is computed for Case B recombination at T_e =10,000K.

As can be seen from figure 1.7, Hα is a very useful tracer of SFR with a rest wavelength of 6562.8$\AA$. It is not without its limitations however. The method rests on the assumption that all of the massive star formation is traced by the ionised gas and the answers are sensitive to the ratio of high mass stars to low mass stars (and consequently to uncertainties in the IMF). Furthermore, Hα is redshifted out of the visible window in galaxies with z $>$ $\sim$0.5. An alternative line, at a bluer wavelength is the forbidden line [OII]. This is in fact a doublet at 3726.1 and 3728.8$\AA$, usually quoted as the approximate average wavelength of 3727$\AA$. Although the luminosities of forbidden lines are sensitive to metal abundance as well as the ionising luminosity, the excitation of [OII] can be calibrated empirically through Hα as a quantitative SFR tracer.

There is, of course, a difficulty with emission lines. They are hard to obtain, especially

at high redshift, because a lot of telescope time is required for a small number of objects. So, in the unfortunate absence of emission line luminosities, a more crude but useful method is to use galaxies' colour indices. This is simply the galaxy's magnitude at one wavelength (usually the wavelength of a standard filter) subtracted from that at a longer wavelength. Different filters and photometric systems are discussed in more detail in section 1.3.1. Whilst optical colour indices are too degenerate with metal abundance to be calibrated to give precise SFR values (although u-v vs. v-k can break the metal degeneracy to some extent), they are still able to indicate broadly what type of galaxy is being observed. For example, as described above, bluer galaxies tend to comprise younger stars and are more likely to be spirals. Redder galaxies are more likely to comprise older stars and are more likely to be elliptical. To probe SFR, colour indices that have one filter either side of the 4,000$\mathring{A}$ break at the redshift of the galaxy are more useful. Emission line luminosities are most likely to be unavailable for faint galaxies and this is when colour indices are most likely to be the only tool to hand.

It is worth mentioning at this point that, in theory at least, it is possible to simulate the evolution of galaxy colours. With an accurate initial mass function (IMF), an analytic form of the star formation history of the galaxy, a theory of stellar evolution that incorporates nucleosynthesis and metal yields and a vast spectral library, the various colour indices and line fluxes of a particular galaxy can be computed for any epoch. Two of the best attempts to do this have been the stellar population synthesis models of Bruzual & Charlot (e.g. [12]) and the project called Projet d'*Étude* des GAlaxies par Sythese *Évolutive* (P*ÉGASÉ*, [37]). These synthesised colours provide a useful reference (within inherent uncertainty) against which to compare measured colours.

1.2.4 The Decline in SFR

It has long been known (e.g. [59]) that the cosmic star formation rate has dropped significantly since the universe was approximately half of its current age. In fact, the star formation rate (SFR) is believed to have dropped by a factor of 3-10 since z $\sim$ 1-2. Figure 1.9 shows the variation of star formation rate density (SFRD) with redshift. The figure shows the rate for all galaxies and also for galaxies of different masses. It is natural to ask why this drop in SFR has happened. The possible answers can

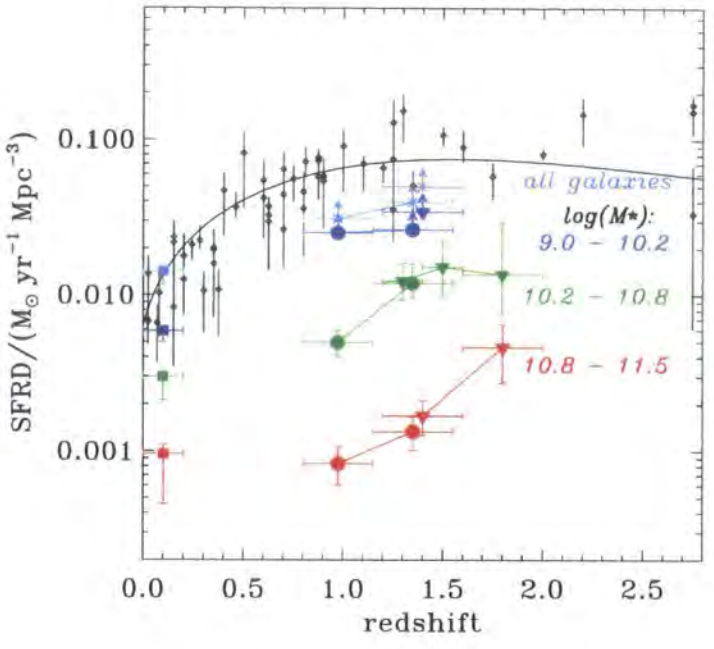

Figure 1.9: SFRD (from [50] derived from L([OII]) (circles) and from L(2,000Å) (triangles). The diamonds are the values derived in [44]. The solid line is the fit derived in [17].

be broadly divided into two categories: those that rely on processes intrinsic to the galaxies that are hosting the star formation and those that rely on extrinsic processes.

Intrinsic Processes

The most likely intrinsic process for the decline in a galaxy's star formation rate is that the available gas from which to form stars diminishes as more stars are formed. The following very simple example shows how the assumption of an SFR that is proportional to the amount of gas available for SF leads directly to an exponentially declining SFR. Consider a cloud of gas of constant mass M_0. Let $M_\star(t)$ be the mass that is in stars at time t and let M(t) be the mass that is not in stars at time t. Then

$$M_\star(t) + M(t) = M_0 = constant \tag{1.15}$$

Then

$$\dot{M}_\star = -\dot{M} \tag{1.16}$$

and the above assumption yields

$$\dot{M}_\star \propto M = kM \tag{1.17}$$

Substituting equation 1.17 into equation 1.16 then yields

$$kM = -\dot{M} \tag{1.18}$$

giving

$$\int \frac{dM}{M} = -k \int dt \tag{1.19}$$

Then integrating gives

$$M = M_0 e^{-kt} \tag{1.20}$$

and finally

$$M_\star = M_o(1 - e^{-kt}) \tag{1.21}$$

and

$$\dot{M}_\star = ke^{-kt} \tag{1.22}$$

Thus, as a simple model, the exponentially decaying SFR is a good starting point. An alternative to the ideas presented above would be to have a homogeneous "blob" of gas of density ρ. Now consider the Schmidt law that relates the SFRD to the mass density:

$$\rho_{SFR} \propto \rho_{gas}^n \tag{1.23}$$

where ρ_{SFR} and ρ_{gas} are the volume densities of star formation and gas.

Then, the SFRD is determined by the density of the gas that is available to form stars. Kennicutt [53] found that 1.5 was a physically plausible value for n. This prediction came from a picture in which the large-scale SFR is presumed to scale with the growth

rate of perturbations in the gas disk. Assuming a constant volume and substituting equation 1.23, with n=1.5, into equation 1.16 yields

$$\dot{M}_\star \propto t^{-3} \tag{1.24}$$

Another mechanism by which a galaxy loses gas is via the superwinds from typeII supernovae. Whether this gas will actually escape the galaxy will depend on, amongst other things, the mass of the dark matter halo and modelling such a phenomenon is far beyond the present scope. For much more advanced models, see, for example, [69] and [54].

However, there are several possible mechanisms originating from outside a galaxy that could theoretically suppress or even cut off the star formation [11].

Extrinsic Processes: Ram Pressure Stripping

"Ram pressure stripping" was first proposed as an active mechanism in cluster cores back in 1972 [41]. Via force balance considerations, they estimated that a galaxy moving through a hot, ionised intra-cluster medium (ICM) would experience a "ram pressure" from the ICM that could potentially strip away most or even all of the gas in the disk of the galaxy. This mechanism has recently been invoked to explain the rapid rise in the ratio of lenticular (S0) galaxies to spirals since z=0.5 that was noted by [22]. Ram pressure stripping provides a mechanism for turning gas rich spirals in cluster cores into the featureless disky S0s with no atomic hydrogen left that are found today. They have no recent star formation but have evidence of a sudden halt in the star formation in the past. Figure 1.10 shows a simulation of a disk moving through the ICM at two different angles to the orientation of the disk. The most striking feature is the short time (~100Myr) in which all of the HI is removed. The mechanism of ram pressure stripping is only effective in a dense environment and is more so for faster moving galaxies. The ram pressure is proportional to $\rho_{ICM} v_{gal}^2$ where ρ_{ICM} is the density of the ICM and v_{gal} is the velocity of the galaxy.

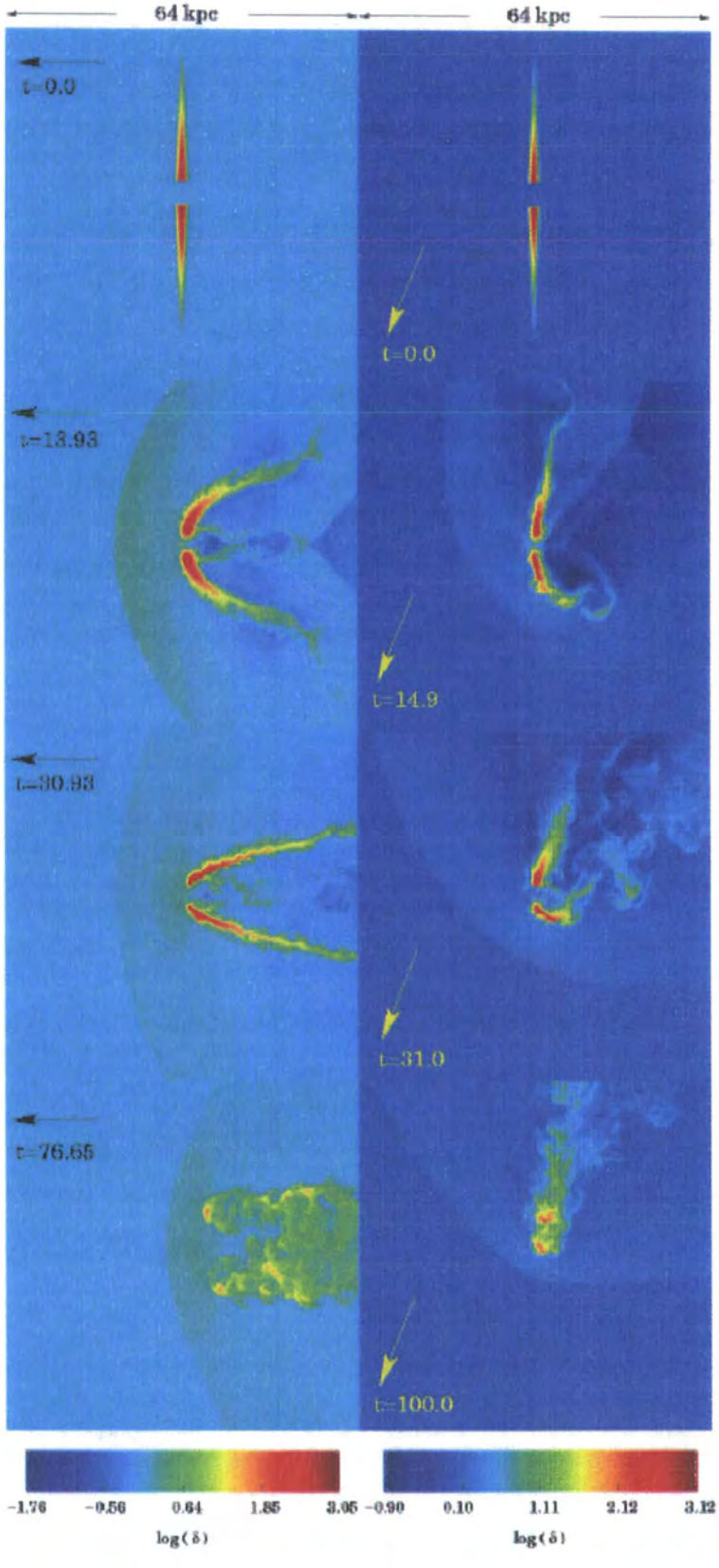

Figure 1.10: The evolution of a gaseous disk of a spiral galaxy moving face on (left column) and inclined at 20^0 to the direction of motion (right column) through a diffuse, hot intra-cluster medium. The galaxy is moving at 2000kms^{-1} through an intra cluster medium (ICM) of density 2600 $h_{50}^{1/2}$ atoms m^{-3}. Each frame is 64kpc on one side. Perhaps surprisingly, 100% of the HI disk is lost within 100Myr. [66]

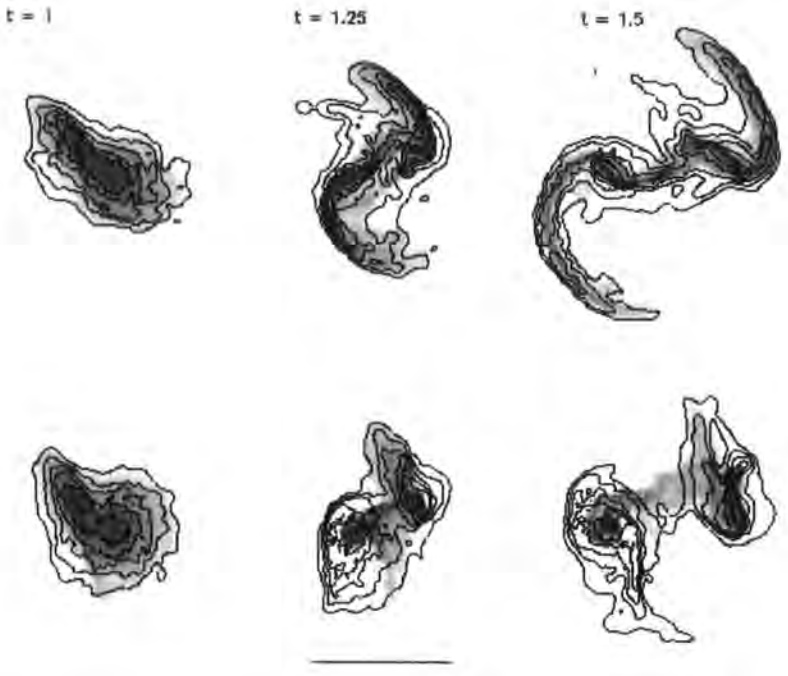

Figure 1.11: Simulations of a direct encounter (top) and a retrograde encounter (bottom) between two galaxies of equal mass. The grey scale shows logarithmic gas surface density. The contours show stellar surface density in steps of one magnitude. [5]

Extrinsic Processes: Collisions and Harassment

A second mechanism is collisions and harassment. The tidal forces produced by the gravitational interaction of two galaxies that pass near to each other are likely to channel gas towards the galactic centre [5]. This may cause a starburst which in turn will eject a large fraction of the gas from the star forming region. Also, the gas in the outer parts of the galaxy will be drawn away. This process will be most effective in environments where the timescale of the encounter is similar to that of the orbital period within the galaxy. Although this is most likely in groups, [62] showed the cumulative effect of many weak encounters can also be important in clusters of galaxies. Figure 1.11 shows simulations of how equal mass galaxies may interact when they pass each other closely with direct geometry (top row) and with retrograde (i.e. spinning in opposite directions) angular momentum (bottom row). See [5] for details.

Extrinsic Processes: Strangulation

Thirdly, a galaxy's star forming region can be "strangled" (e.g. [58]). An isolated star forming galaxy gets its baryons from a reservoir in its halo. When it joins a group of

galaxies, it may lose its position at the centre of this reservoir and the supply of fresh gas will be reduced.

It is thus very important to understand the role played by the galaxies' environment in the declining SFR and this work aims to shed some light on this issue.

1.2.5 Red and Blue Galaxies

For the rest of this thesis, I shall talk about galaxies as though they only populate two groups: reds and blues. It is a simple model but one that has its benefits. For example, one can measure the relative abundances of these two groups at different redshifts and in different environments with only galaxy colours to hand. One can consider whether galaxies are moving from one group to another, when that's happening and what's causing them to do so. In short, splitting galaxies in this way enables an investigation of the evolution of the dependence on parameters such as environment of galaxies' SFR in the absence of spectral lines.

This simple splitting of the galaxies into two groups is further justified when one looks at the colour distribution of galaxies from a survey. Two distinct populations, one with redder colours and one with bluer colours, are seen. This trend in galaxies in the local universe has been known for some time [3] but it has recently been seen out to $z \sim 1$ [6]. In this sense, measuring a galaxy's colour is a very powerful tool with which to study star formation. Colours are readily quantifiable, easily reproducible and, via the models such as those mentioned above, directly related to star formation history without making further assumptions. Further, as mentioned above and as shown in several figures throughout this work, the colour distribution is bimodal. When investigating galaxies using unimodal functions, the galaxies will tend to populate a single clump in the given parameter space [30]. It is then difficult to track how galaxies evolve. When the parameter space clump is divided up into smaller parts, it is not clear whether a change in the number of galaxies in a particular bin is due to a change in the number of galaxies or to the motion of galaxies in and out of that bin from neighbouring bins. Although other parameters can be bimodal, colour remains the easiest to measure and it's also relevant to the emergence of the Hubble sequence.

[4], hereafter B04, studied the distribution of galaxy colours, as a function of both

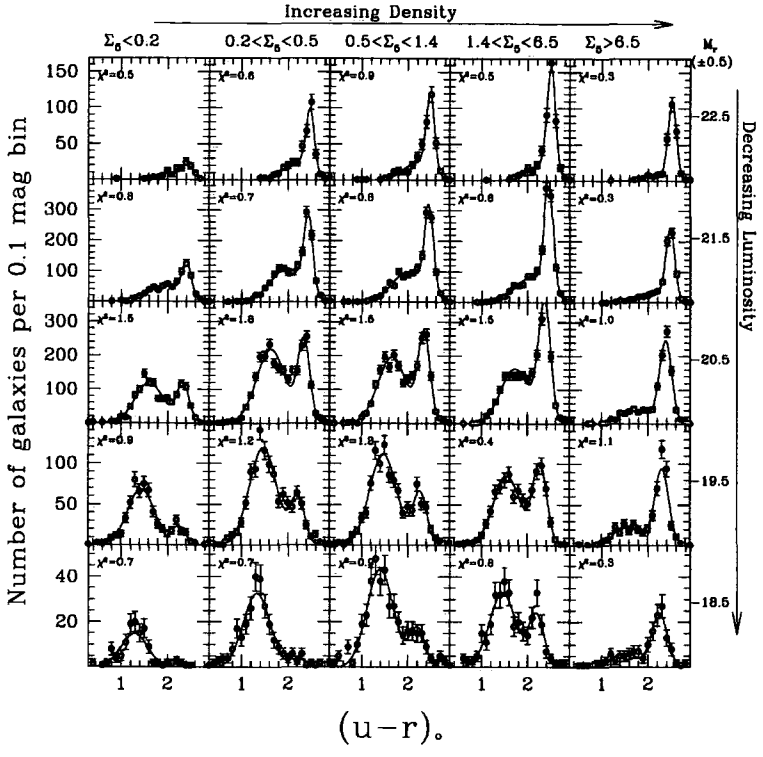

Figure 1.12: (From B04; SDSS galaxies). The distributions of u'-r' colours in luminosity and density bins. The distributions are again clearly bimodal

environment and luminosity, in the local universe. Figure 1.12 shows a 5x5 block of histograms of galaxies' u'-r' colours. The data are taken from the SDSS. It is immediately apparent from this figure that, at any given luminosity, the fraction of galaxies that are red increases with increasing environmental density (I discuss in detail how environmental density is quantified in §3). However, at a fixed environmental density, the mean colours of each of the red and blue distributions does not change much at all with increasing galactic luminosity. This is shown more clearly in figure 1.13 which plots, for each of the red and blue distributions, the mean colours of those distributions as a function of density, with one line for each of the five luminosity classes. Figure 1.14 shows clearly the increasing fraction of galaxies that are red with increasing environmental density in all luminosity classes.

The following questions naturally arise: does the cluster environment cut off star formation? If the cosmic SFR was highest around z∼1, what was the environmental dependence of the colour distribution at that time? Since z∼1, how have galaxies' environments changed? Can any change in the colour distribution (and hence the SFR) since z∼1 be accounted for by the change in environment? This work aims to answer

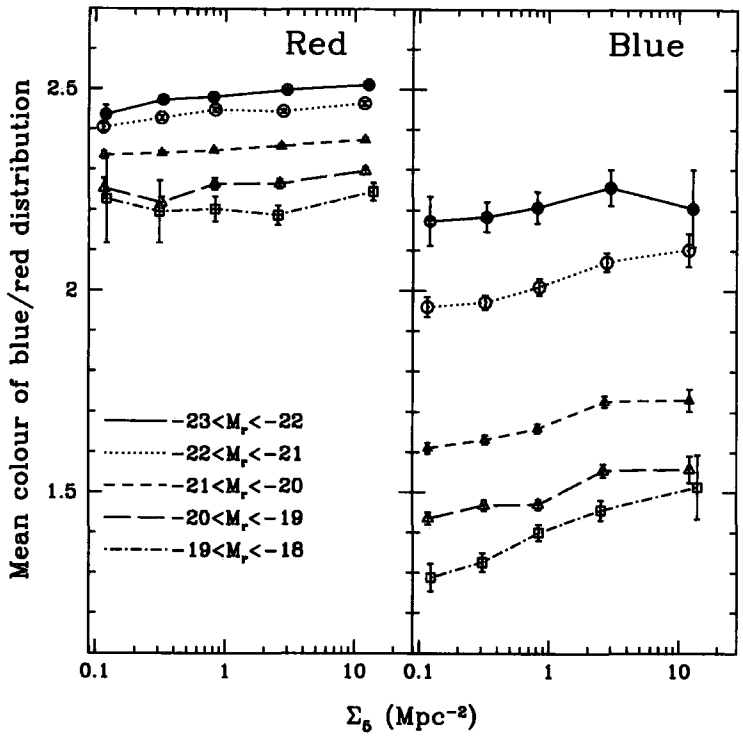

Figure 1.13: (From B04, SDSS galaxies). The mean colours of the red and blue distributions divided into their luminosity bins.

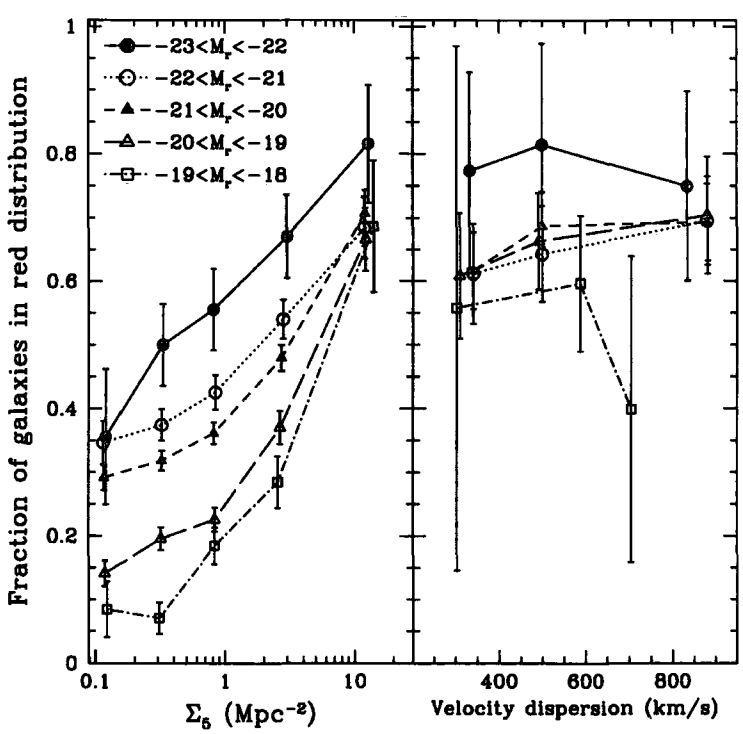

Figure 1.14: (From B04, SDSS galaxies). The fraction of galaxies that are red, as a function of density (left panel) and velocity dispersion (right panel), both divided into luminosity bins.

these questions by carrying out a similar analysis to B04 but at z$\sim$1 and then comparing the colour distributions and environmental dependences of the colours at the two different epochs. In §2 I describe the current status of high redshift galaxy surveys, the data used and how a volume limited sample was made. In §3 I review different methods of measuring environmental density and describe the way in which I analysed the data and how the errors were estimated. In §4 I describe my results and present an argument describing what caused the changes in colour between the two epochs. There is a discussion, along with my conclusions, in §5.

1.3 Galaxy Photometry

Just before moving on to the part of this thesis describing my own work, it is necessary to explain a few points regarding how astrophysicists analyse photons from distant galaxies so that they can compare the galactic colours they infer with those of other researchers. In this section, I shall firstly describe the different photometric systems in use. It is important to remember that older photometric systems such as the Johnson system are not based on SI units but use the magnitude of Vega in various wavebands as a calibration. Later systems, such as the SDSS system use the AB magnitude system. This is a big step in the right direction with regard to SI units because the flux corresponding to 0 magnitude is the same in all bands. After describing magnitude scales and the different photometric systems,I shall then describe K-corrections and E-corrections.

1.3.1 Photometric Systems

The curious, arbitrary nature of the stellar magnitude scale is due to its historical development. Almost 2,000 year ago, Hipparchus defined a qualitative scheme in which stars visible with the naked eye fall into six brightness categories. The scheme was later refined by Ptolemy. The brightest stars were designated first magnitude and the faintest sixth magnitude. William Herschel's finding that a first magnitude star was 100 times brighter than a sixth magnitude star was verified by N. R. Pogson in 1856 and the scale was quantified. Therefore an interval of five magnitudes corresponds to a factor of 100

in brightness and a one magnitude interval corresponds to a brightness ratio of $100^{1/5}$ = 2.512. In fact, this definition reflects the operation of the human eye which translates equal ratios of actual intensity into equal ratios of perceived intensity. The human eye is therefore a logarithmic detector. Consider two stars m and n with fluxes f_m and f_n and apparent magnitudes m and n respectively. Since a one magnitude difference means a brightness ratio of $100^{1/5}$, (m-n) magnitudes mean a ratio of $(100^{1/5})^{m-n}$. Therefore,

$$f_n/f_m = 100^{(m-n)/5} \tag{1.25}$$

Taking logarithms (to the base 10) of both sides and then rearranging then yields:

$$m - n = 2.5log(f_n/f_m) \tag{1.26}$$

The absolute magnitude of an object is defined as the magnitude that would be observed if the object were placed at a distance of 10pc from the Sun. The colour of an object (and more pertinently for the current work, a galaxy) is given by the difference between its magnitudes at two different wavelengths. It is usual to use colour = (magnitude at a shorter wavelength) - (magnitude at longer wavelength) such that, the more positive the colour, the redder it is and, the more negative the colour, the bluer it is. In practice, magnitudes are only available at certain fixed wavelengths where standard filters are used. Thus, to define a photometric system, one needs a detector, a set of filters and a means of calibration.

1.3.2 The Johnson-Morgan-Cousins Photometric System

Until recently, the photometric system that was almost ubiquitously used was that of Johnson and Morgan [49] and Cousins [19]. Their filters' parameters (effective wavelength, λ_0, and bandpass, $\Delta\lambda$) are shown in table 1.1.

For the system to be really useful, it must be calibrated. The first stage of the calibration requires a large set of stars (Johnson and Morgan used about 100 stars for their initial calibration). It is necessary to determine the apparent magnitude of every star relative to every other, thus defining the standard magnitudes of the photometric system (i.e. filters and detector). Then, in the second stage, the absolute flux of just

Filter	λ_0	$\Delta\lambda$
U	365nm	70nm
B	440nm	100nm
V	550nm	90nm
R	640nm	150nm
I	790nm	150nm
z	950nm	200nm
J	1.25μm	0.12μm
H	1.66μm	0.16μm
K	2.22μm	0.22μm
L	3.45μm	0.35μm
M	4.65μm	0.46μm
N	10.3μm	1.0μm

Table 1.1: The names, central wavelengths and typical passbands of the filters used in the Johnson photometric system

one star is calibrated, usually given for zero magnitude at each filter, and the whole system is calibrated. The star chosen for this purpose was Vega. This means that Vega has magnitude 0 in every band of the photometric system, even though it has different levels of flux (for example measured in SI units) in each band.

Apparent magnitudes in the Johnson/Vega system are denoted by capital letters (e.g. B, V) and absolute magnitudes are subscripted (e.g. M_B, M_V).

1.3.3 The SDSS Photometric System

There have been several other magnitude systems developed over the years, one of which is the SDSS photometric system. In 1995, ahead of the first data release from the huge Sloan Digital Sky Survey, a new photometric system (also known as the AB_{95} system) was developed based on the filters and detector of that survey. The system comprises five colour bands: u', g', r', i' and z'. (Notice that colours and magnitudes in this system are denoted by lower case letters and apostrophes, unlike those in the Johnson system). Table 1.2 gives the effective wavelengths and passbands of these

Filter	λ_0/nm	$\Delta\lambda$/nm
u'	350	60
g'	480	140
r'	625	140
i'	770	150
z'	910	120

Table 1.2: The names, central wavelengths and typical passbands of the filters used in the SDSS photometric system. Note that the shape of the z' response function at long wavelengths is determined by the CCD sensitivity.

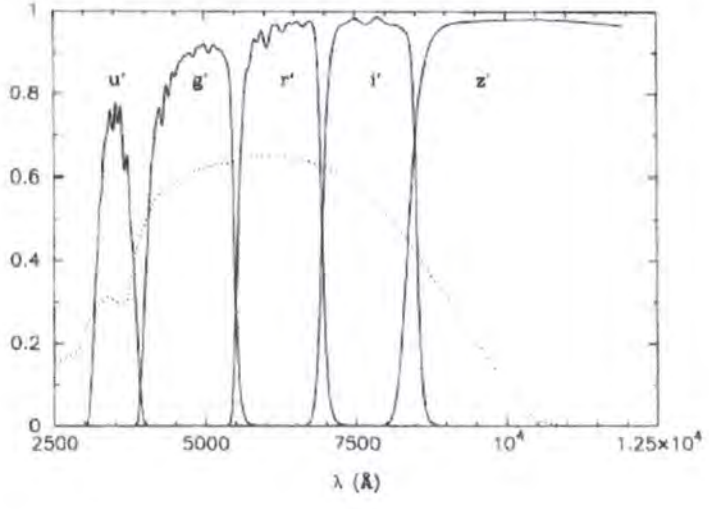

Figure 1.15: Transmission of the SDSS u', g', r', i', z' filters. The dotted curve is the quantum efficiency of a thinned UV-coated SITe CCD; this is the detector that is used in the definition of the SDSS system. [38].

filters [38] and the response curves are shown in figure 1.15.

The zero point of this system is the AB_v system of [63]. The key difference between this system and the Johnson system is that here the flux corresponding to 0 magnitude is the same in all bands. Another notable feature of the SDSS photometric system is the large width of the filter bandpasses. There is a trade-off in the choice of bandwidth. The larger it is, the more flux is admitted to the detector but less spectral information is provided. The SDSS filters ensure high efficiency for faint object detection and essentially cover the entire accessible optical wavelength range. The filters also have particularly sharp wavelength cutoffs due to the variation of the optical index within

the thin films they're made from.

1.3.4 The Kron Photometric System

In this section, I describe Kron's approach to determining a galaxy's magnitude. Kron [57] considered the problem of how much of a resolved galaxy's light should be included in the calculation of its magnitude. Obviously, in a perfect world, all of it would be but the greater the radius out to which one integrated the flux, the noisier the measurement will be. Kron simply wanted to put down a circular aperture, measure the flux within it and then subtract the background. It is obviously important to accurately model the intensity profile of the galaxy, which is where I shall start this description.

In 1963, Sérsic generalised de Vaucouleurs' (e.g. [20]) $R^{1/4}$ model (for the distribution of a galaxy's intensity) to his own $R^{1/n}$ model (e.g. [68]). Sérsic's intensity profile is expressed as

$$I(r) = I_e exp\left\{ -b_n\left[\left(\frac{R}{R_e}\right)^{1/n} - 1\right]\right\} \tag{1.27}$$

where I_e is the intensity at the effective radius R_e that encloses half the total light and b_n is a constant that is defined in terms of n. See [40] for details.

In 1980, Kron [57] developed a magnitude system (Kron magnitudes that derive from Kron radii) that can take an intensity profile such as that in equation 1.27 and can return galaxy magnitudes. The Kron radius, R_1 is defined as follows:

$$R_1(R) = \frac{2\pi \int_0^R I(x)x^2dx}{2\pi \int_0^R I(x)xdx} \tag{1.28}$$

where x is the dummy variable for radius, I(x) is the intensity profile and R is the radius out to which the integration is calculated. R_1 is thus a luminosity-weighted radius that defines the "first moment" of the image. The question to be answered is how many effective radii must one integrate out to in order to have included enough of the galaxy's flux from which to derive a magnitude. Consider the analysis below: using a Sérsic intensity profile and substituting in

$$x = b\left(\frac{R}{R_e}\right)^{1/n} \tag{1.29}$$

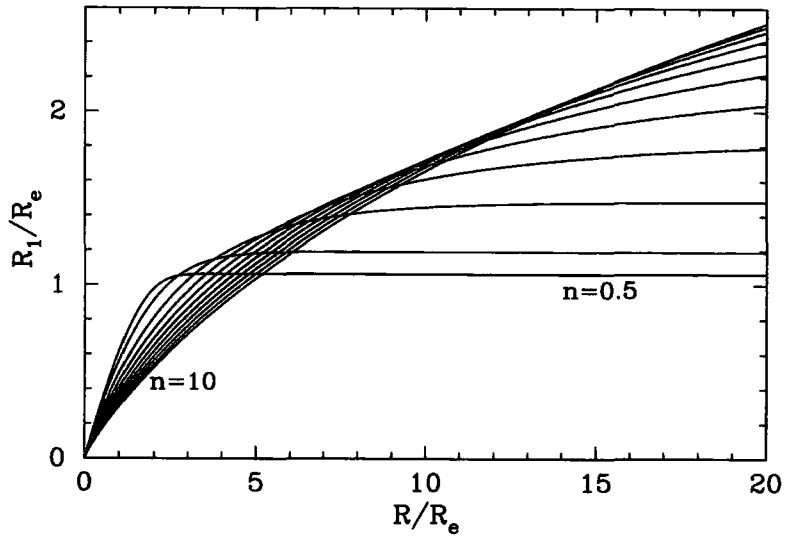

Figure 1.16: Kron radii R_1, as obtained from equation 1.30, are shown as a function of the radius R to which the integration was performed. Values of n range from 0.5, 1, 2, 3, ... 10. [40]

Then equation 1.28 can be rewritten as

$$R_1(x,n) = \frac{R_e}{b^n}\frac{\gamma(3n,x)}{\gamma(2n,x)} \tag{1.30}$$

where

$$\gamma(R) \equiv \frac{-d[logI(r)]}{d[logR]} \tag{1.31}$$

Kron argued, without rigorous derivation, that an aperture of $2R_1$, when R_1 was obtained by integrating out to a radius R that is 1% above the sky flux, contains more than $\sim$ 90% of an object's total light. Indeed, the SExtractor software [8] integrates out to $2.5R_1$. However, figure 1.16 shows a plot of R_1 vs. R, both in units of R_e for various values of n. It is clear from this plot that, given that one usually only measures a light profile out to 3-4 R_e at best, the asymptotic value of (R_1/R_e) (i.e. that value that cannot be increased, even by integrating out to greater and greater radii) will only be approached for profiles with n less than about 1. Table 1.3 gives values of the asymptotic values of (R_1/R_e) for the different values of n and also the percentage of the luminosity that is included in $2R_1$ and $2.5R_1$. It is from these luminosities that the Kron magnitudes are calculated.

Sérsic n	Asymptotic R_1/R_e	L(<2R_1) %	L(<2.5R_1) %
0.5	1.06	95.7	99.3
1.0	1.19	90.8	96.0
2.0	1.48	87.5	92.2
3.0	1.84	86.9	90.8
4.0	2.29	87.0	90.4
5.0	2.84	87.5	90.5
6.0	3.53	88.1	90.7
7.0	4.38	88.7	91.0
8.0	5.44	89.3	91.4
9.0	6.76	90.0	91.9
10.0	8.39	90.6	92.3

Table 1.3: Theoretical Kron radii and magnitudes [40].

1.3.5 The Petrosian Photometric System

The final photometric system that I shall mention is that of Petrosian [65]. Petrosian defined a quantity η(R) such that

$$\eta(R) = \frac{2\pi \int_0^R I(R')R'dR'}{\pi R^2 I(R)} \tag{1.32}$$

$$= \frac{L(< R)}{\pi R^2 I(R)} = \frac{\langle I \rangle_R}{I(R)} \tag{1.33}$$

The logarithmic expression, plotted in figure 1.17, is written:

$$2.5log[\eta(R)] = \mu(R) - \langle \mu \rangle_R \tag{1.34}$$

where μ(R) is the surface brightness profile. η(R) is thus the average intensity within some projected radius R divided by the intensity at that radius. η(R) is actually a very useful function because, if every galaxy had the same stellar distribution, for example a Sérsic $R^{1/n}$ profile with the same value of n for each galaxy, then a radius where the η-function equalled some pre-defined, constant value would correspond to the same number of R_e for every galaxy. The flux within R_P, when $1/\eta(R_P) = 0.2$, is

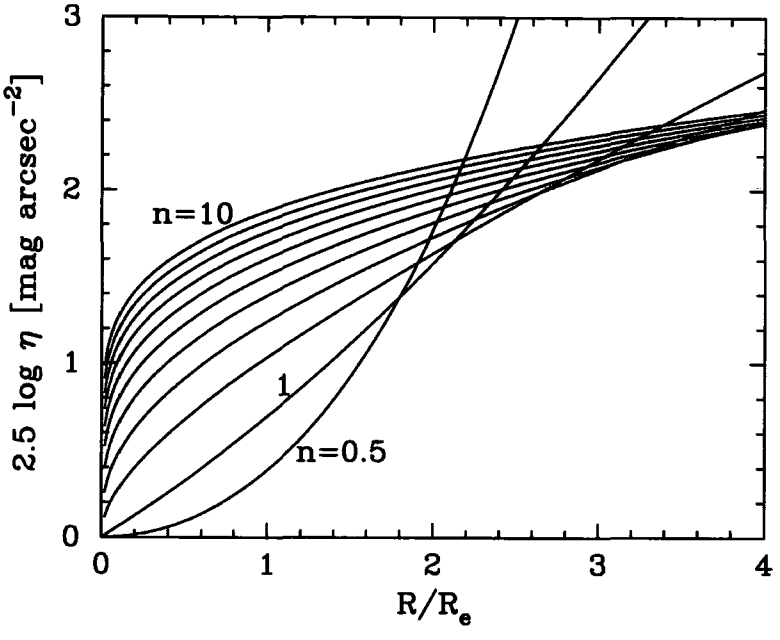

Figure 1.17: The logarithm of the Petrosian function $\eta(R)$ given by equation 1.34, shown as a function of normalised radius (R/R_e) for Sérsic profiles having n = 0.5, 1, 2, 3, ..., 10. [40]

often used to estimate an object's flux. The advantages of this method are that the measurements are unaffected by exposure-depth (i.e. the limiting surface brightness detected) and cosmological redshift dimming because these effects affect both surface brightness terms in equation 1.34 equally. See [40] and references therein for details.

1.3.6 K-Corrections

In Hubble's universe, space is expanding and thus galaxies are moving apart from each other. Note that, in this section, I shall not be concerned with galaxies' peculiar velocities, only their velocities due to the Hubble flow. The light that reaches us from these distant galaxies is thus redshifted. To view this light with a telescope on Earth, one must use a filter whose wavelength window includes the wavelength of the redshifted light, not as it would appear in the rest frame of the emitting galaxy. The resultant spectral energy distribution (SED, a plot of emitted luminosity versus wavelength) will be similarly redshifted. A "K-correction" must be used to change the SED to that which would be seen by an observer in the rest frame of the galaxy that emitted the photons. In a perfect world, this would be simple. One would deduce the redshift of the galaxy from the emission and/or absorption lines in the spectrum then simply

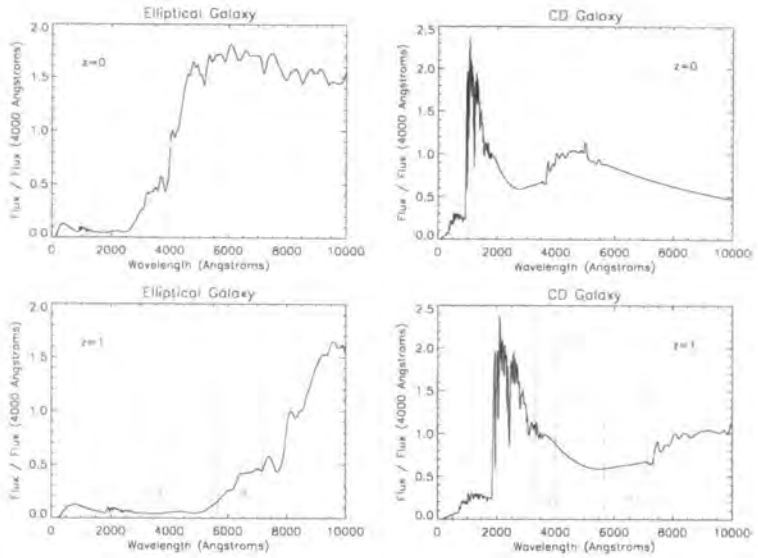

Figure 1.18: Plot showing the typical SEDs (relative to the Johnson U and R filters) of an elliptical galaxy and a cD galaxy as seen at z=0 and at z=1. The fluxes have been normalised to those at 4000$\AA$ in the rest frame in all 4 plots. Note: the SEDs in this figure are low resolution and do not show every spectral feature. They are those of Coleman, Wu and Weedman [18]

divide all the wavelengths by (1+z). However, the situation is significantly complicated by the transmission function of the filter used at the redshifted wavelengths. This will vary non-linearly with wavelength.

Figure 1.18 shows what parts of the typical spectra of elliptical and cd galaxies would be seen though the U and R filters in the rest frame (z=0) and at z=1, where the emitted wavelengths are multiplied by 2 to give the observed wavelengths. In practice, K-corrections would normally be made just to a galaxy's various colours (i.e. its absolute magnitude in one waveband subtracted from that in another band of longer wavelength) or to the absolute magnitudes themselves, rather than trying to recover the whole SED. As can be seen from figure 1.18, the ratio of the fluxes in the two filters for a given galaxy type is not necessarily constant between the two epochs but in fact depends on the galaxy's SED (and thus its star formation history, SFH). Thus the K-correction is also SFH dependent.

Section 2.2.2 briefly describes how the K-corrections were done with the Groth Strip galaxies.

1.3.7 E-Corrections

A further correction to galaxy colours, required to account for the evolution of the galaxy during the time between emission and detection of its photons, is known as the e-correction. In other words, if a galaxy's colour is observed at high redshift and one wants to know how that colour would appear today, it is necessary to estimate how many of its stars would have moved off the main sequence, become redder, etc. However, it should be noted that such a correction does not account for new stars being formed in the galaxy which will also alter its colour. The e-correction is thus limited in its use.

Chapter 2

Data

2.1 Overview of Current High Redshift Surveys

In this section I present an overview of the current status of high redshift galaxy surveys. Table 2.1 summarises the surveys' key parameters. High redshift surveys aim to complement the low redshift surveys, primarily the SDSS and the 2DFGRS, and the CMB data by providing information about the universe at an intermediary epoch. They aim to shed light on some of the fundamental questions in modern cosmology. For example, by providing statistics of large scale structure to be compared to the other epochs, the surveys will help to show the evolution of large scale structure and how that has depended on the distribution of dark matter.

High redshift galaxy surveys are also able to provide evidence as to the value of the cosmological constant, Ω_Λ. Non zero values of Ω_Λ would warp spacetime in predictable ways which affect the relationship between the apparent size, brightness and number of galaxies versus redshift. These are the things that high redshift surveys can measure.

2.1.1 The Deep Extragalactic Evolutionary Probe (DEEP) survey

The DEEP survey is a multi-year programme (observing from 2001 to 2005) which uses the twin 10m W.M. Keck Telescopes and the Hubble Space Telescope (HST) to conduct a large scale survey of distant, faint, field galaxies. Their broad scientific goals

Name	Telescopes	Instruments	Redshift Range	Area of Coverage	Magnitude Limit & Band
DEEP1 (Groth Strip)	Keck	LRIS	0.2 - 1.2	1 × 40' × 5' = 0.056 $\square^0$	24.0 (I)
DEEP2	Keck	DEIMOS	0.70 - 1.55	4 × 120' × 16' =2.16 $\square^0$	24.5 (I_{AB})
GDDS	2 × Gemini	GMOS	1 - 2	4 × 30 $\square$' = 0.033 $\square^0$	24.5 (I_{AB})
VVDS	VLT	VIMOS	0 - 5	4 × 2^0 × 2^0 = 16 $\square^0$	26 (I_{AB})
GOODS	SST, HST, Chandra, XMM-N	Various	1 - 6	300 $\square$' = 0.833 $\square^0$	Various
zCOSMOS	VLT	VIMOS	1.2 - 2.4		25 (B_{AB})

Table 2.1: Summary of the current high redshift galaxy spectroscopic surveys. Acronyms are as follows: DEEP - Deep Extragalactic Evolutionary Probe, GDDS - Gemini Deep Deep Survey, VVDS - Vimos VLT (Very Large Telescope) Deep Survey, GOODS - Great Observatories Origins Deep Survey, LRIS - Low Resolution Imaging Spectrograph, DEIMOS - DEep Imaging Multi Object Spectrograph, GMOS - Gemini Multi Object Spectrograph, CFHT - Canada France Hawaii Telescope, VIMOS - VIsible Multi Object Spectrograph, SST - Spitzer Space Telescope, HST - Hubble Space Telescope, XMM-N - X-ray Multi Mirror - Newton

include investigating the formation and evolution of galaxies, the origin of large scale structure, the nature of the dark matter, and the geometry of the Universe.

Another issue is that of the galaxy bias. The problem is that, since it is believed that the conversion of baryonic gas into galaxies and stars was inefficient and uneven throughout the universe, the resulting galaxies are an imperfect tracer of dark matter. A way of attacking this problem is provided by the DEEP survey. It will measure galaxies' line widths from which their (visible) masses can be inferred. Although the galaxy formation models will probably not be able to infer the mass of an individual galaxy's dark matter halo from its visible mass accurately enough, it is hoped that, over large scales, the fluctuations will average out leaving an offset that is just a scale factor. Thus an extra tool is provided in turning maps of (luminous) galaxies into maps of dark matter. DEEP will also investigate the nature of dark matter (i.e. is it hot or cold?) by measuring the power spectrum on short length scales (150 million light years) which are highly diagnostic for distinguishing hot from cold dark matter.

There are two phases to the DEEP project. The first phase, DEEP1 incorporates 3 main fields and other small patches, one of which is the Groth Strip (GS). The data that I have used in this work are from the GS. DEEP1 was a pilot phase for DEEP2 which uses the DEIMOS spectrograph on Keck to obtain redshifts of $\sim$ 50,000 faint galaxies with redshifts > 0.7. Examples of recent results from the DEEP survey include the following: only 9% of present day L* galaxies have undergone major mergers since $z \sim 1.2$ [32]; the discovery of luminous, metal-poor galaxies at redshifts ~ 0.7 [31]; finally, [28] analysed clustering of galaxies and of groups of galaxies at $z \sim 1$. They found that groups are more clustered than galaxies and that galaxies in groups are more clustered than the full galaxy sample.

2.1.2 The Gemini Deep Deep Survey (GDDS)

The GDDS is an ultra-deep ($K < 20.6$ mag, $I < 24.5$ mag) redshift survey targeting galaxies in the "redshift desert" between $1 < z < 2$. The primary goal of the survey is to constrain the space density at high redshift of evolved high-mass galaxies [1]. Recent results from the survey include: evidence for a significant population of red galaxies at $1.3 < z < 2.2$ whose integrated light is dominated by evolved stars [61]; the finding that

a significant fraction of massive galaxies were formed just 3Gyr after the big bang [39]; the statistical properties of the heavy element enrichment in the interstellar medium (ISM), including high FeII column densities, of star forming galaxies at redshift 1.3 < z < 2 [67].

2.1.3 The Vimos VLT Deep Survey (VVDS)

The VVDS covers a large area of the sky (16 $\square^0$) and also a large redshift range (0 < z <5). It aims to "set major constraints onto galaxy formation models, large scale structure formation models and cosmological scenarios describing the evolution of the universe". Their strategy has been as follows: firstly, deep imaging of the whole area of the sky was obtained in UBVRI and also in K in some selected areas. Then redshifts were obtained for galaxies in magnitude selected samples from the imaging survey. These samples ranged from the shallowest, 100,000 galaxies down to $I_{AB} = 22.5$, to the deepest, 1,000 galaxies down to $I_{AB} = 26$. Results to date include: the optical and near-infrared identification of 1054 radio sources in the 20cm Very Large Array (VLA) radio survey. It appears that radio selection preferentially selects galaxies with higher intrinsic optical luminosity [27]. [2] measured the evolution of the galaxy luminosity function at 1500$\mathring{A}$ in the redshift range 0.2 < z < 1.2. In addition to confirming that star formation was significantly higher in the past, they found that the bluest class of galaxies evolved less strongly in luminosity than the other classes.

2.1.4 The Great Observatories Origins Deep Survey (GOODS)

GOODS is a follow up to NASA's "Great Observatories" programme. This programme originally comprised four space-borne missions observing at different wavelengths. In chronological order of launch, these were the Hubble Space Telescope (HST) which operates at ultra violet (UV), optical and the near infra-red (NIR),the Compton Gamma-Ray Observatory (CGRO), the Chandra X-Ray Observatory (CXO) and the Spitzer Telescopes that observes in the IR. The project aims to "incorporate a Spitzer Legacy project designed to study galaxy formation and evolution over a wide range of redshift and cosmic lookback time. The project will trace the mass assembly history of

galaxies, the evolution of their stellar populations, and the energetic output from star formation and active nuclei. GOODS builds on the deepest observations from NASA's other Great Observatories, Hubble and Chandra, and will be done in partnership with astronomers at Gemini and ESO (the European Southern Observatory)... By observing at lambda $>$ 3 um, Spitzer will measure the rest-frame near- and mid-infrared light from objects at $1 < z < 6$, but very deep observations are needed to detect "ordinary" galaxies at these high redshifts".

Recent publications from the GOODS include the following: [35] found that they could account for the majority of the 3.6 μm background by integrating the IR background light in the Hubble Deep Field North (HDF-N) from faint sources. [13] analysed the growth of stellar mass with cosmic time, as partitioned according to galaxy morphology. They found little evolution in the form of the galaxy stellar mass function from $z \sim 1$ to $z = 0$ and evidence that the relevant mass scale (for the transition from late type galaxy to early type) moves to higher mass at earlier epochs. This would support the "downsizing" phenomenon, described in chapter 5.

2.1.5 The zCOSMOS Survey

The final survey is the zCOSMOS survey. zCOSMOS will use 600 hours of Very Large Telescope (VLT) time, using the Visible Multi Object Spectrograph (VIMOS) to yield spectra for (i) approximately 28,000 galaxies at $0.2 < z < 1.2$ selected to have $I_{AB} < 22.5$ and (ii) approximately 12,000 galaxies at $1.2 < z < 2.4$ with $B_{AB} < 25$. The goals of the survey include defining the large scale structure defined by the galaxies out to redshifts $z \sim 2.5$ and use spectral diagnostics (e.g. star-formation rate, reddening, chemical abundance of stars and gas) to characterise individual galaxies and populations.

Recently published results include: [33] examined oxygen gas abundances at $z \sim 1.4$ and found that [OII]-selected $m_{B,AB} < -21.5$ galaxies had high [OIII]/[OII] line ratios, low extinction and low metallicity. This type of spectrum is seen in progressively more luminous galaxies as redshift increases and thus this is evidence to support the downsizing picture.

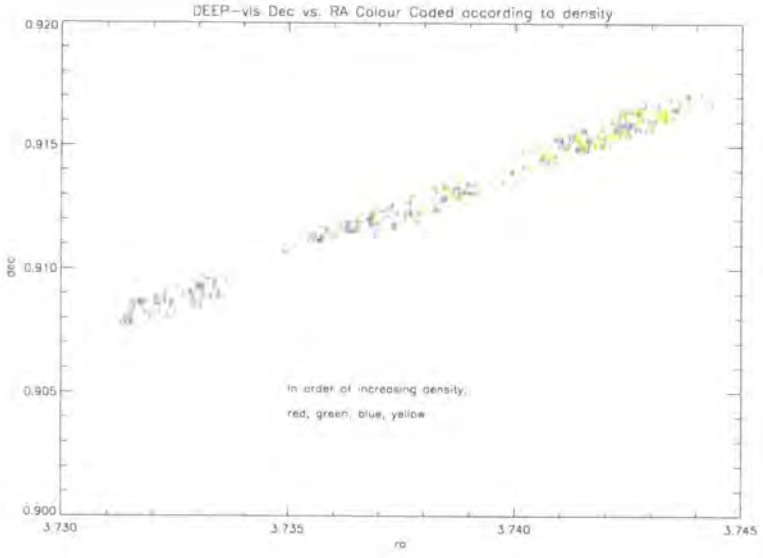

Figure 2.1: The Groth Strip Galaxies' right ascension vs. declination, colour coded according to the density of the local environment

2.2 The DEEP1 (Groth Strip) Data

I took the redshifts, absolute B magnitudes, right ascension (ra) and declinations (dec) from the publicly available catalogue [71]. There were 645 galaxies in the database. The survey was chosen primarily because of the high redshifts of the galaxies ($z_{median} = 0.65$). This would enable a comparison with the local universe that had been explored using the Sloan Digital Sky Survey (SDSS, B04). The strip is shown via the ra/dec distribution in figure 2.1.

2.2.1 The Volume Limited Sample

When constructing a sample of galaxies, there are two types of sample: a magnitude limited sample and a volume limited sample. In a magnitude limited sample, the galaxies are selected according to their apparent magnitudes. i.e. there is a certain magnitude limit (akin to a brightness limit) and only galaxies that are as bright or brighter than this limit are selected. The major drawback with this method is that, whilst bright galaxies both near and far will be included in the sample, fainter galaxies will only be included if they are near. A quick glance at galaxy luminosity functions from any epoch reveals that there are more fainter galaxies than there are brighter ones. Thus, in the region of space from which galaxies have been sampled, not all will be

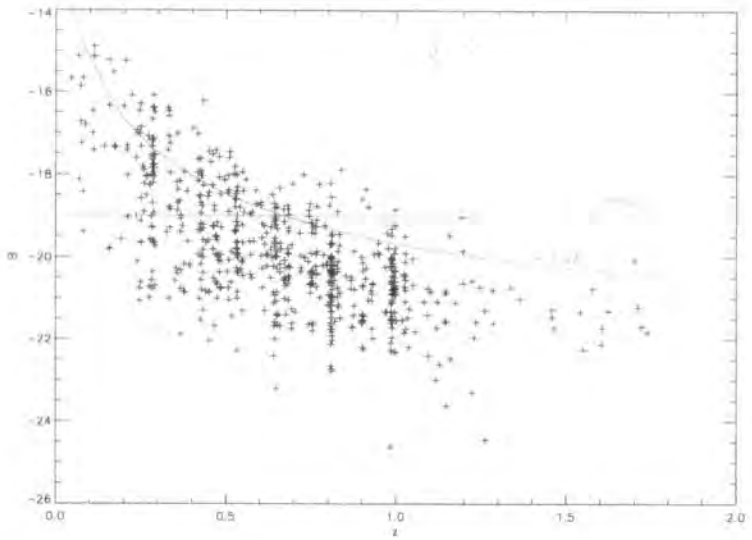

Figure 2.2: Groth Strip galaxies M_B vs. z (magnitude limited sample). The dearth of fainter galaxies at higher redshifts renders the sample unusable for environment studies as it stands

selected. By contrast, in a volume limited sample, all galaxies are selected but only out to a certain distance. This method has the advantage that the survey is (potentially) complete but the disadvantage that it must therefore only sample from a smaller region of space. The Groth Strip survey is a magnitude limited sample and was limited by how faint they could go in the V and I bands. Defining the completeness of the survey as the percentage of galaxies whose redshifts could be determined with a confidence of at least 90%, they found that the completeness declined slowly with magnitude. At (V+I)/2=23, it was at 80%. It dropped to ~50% at (V+I)/2=24 making the effective limiting magnitude of the survey approximately (V+I)/2=24. Figure 2.2 shows the plot of the galaxies' absolute B magnitudes versus redshift. It is clear from the plot that fainter galaxies are simply not seen at higher redshifts.

When studying the environments of galaxies, clearly a sample in which all of a galaxy's neighbours are included is required. I thus needed to make a volume limited sample (vls) out of the magnitude limited sample from the Groth Strip. To do this, I restricted my vls to those galaxies with $M_B < -19.0$ and $z < 1.1$. These values were chosen so as to use a part of the magnitude limited sample where the completeness was maximised. There were 433 galaxies, with a mean redshift of 0.71, in the vls. At the time of this work, this was the largest publicly available, suitable spectroscopic catalogue.

Throughout this work, I assume a ΛCDM cosmology of $(H_0, \Omega_\Lambda, \Omega_M) = (70, 0.7, 0.3)$.

2.2.2 K-Corrections to Groth Strip Data

In this section, I shall provide a brief description of the process used to carry out the K-corrections to the Groth Strip galaxies. See [71] and [36] for fuller descriptions.

In doing the K-corrections, the DEEP team made use of the 34 galaxy UV-optical SEDs (comprising all different morphologies) selected from the atlases of Calzetti et al. [15] and Kinney et al. [55].

The first step in making a K-correction for a particular galaxy (for example at redshift 0.7) was to create synthetic restframe U-B colours for each SED. This was done by convolving the SEDs at z=0 with the response curves of the U and B filters using the U and B zero points in the Vega magnitude system. Secondly, the SED was redshifted to the redshift of the galaxy in question. In the example of the galaxy above, this would mean multiplying all the wavelengths by (1 + 0.7 =) 1.7. This high redshift SED was then convolved with the response curves of the V and I filters (using the same method as was used for the U and B filters above) to produce synthetic high redshift V-I colour. (Light emitted into the U and B filters by a galaxy in the same restframe as the observer would appear in the V and I filters respectively if the galaxy were in the redshift range in question here). Next, the high redshift V-I colours and restframe U-B colours were combined to yield K_{IB}, the K-correction required to change an observed I magnitude at high redshift to a restframe B magnitude (and not to be confused with a K-band magnitude!). Finally, low-order polynomials were used to find each of the U-B colours and V-I colours as a function of K_{IB}. Then entering these fits with the observed V-I colours yields K_{IB} and restframe U-B.

Chapter 3

Analysis

3.1 Methods of Measuring Environmental Density

In this section, I shall briefly overview three different methods of measuring the environmental density (i.e. number of galaxies Mpc^{-3}) in high redshift galaxy surveys. See [29] for more details. In section 3.2, I describe in detail how I measured the densities in my volume limited sample in the Groth Strip data.

All three of the following methods have the advantage that they don't rely on galaxies being put into previously defined classifications of environment. i.e. it is not already assumed that a given galaxy is either in a cluster, a group or in the field. Instead, these methods produce continuous measurements of environmental density.

3.1.1 Cosmological Distances

The n^{th} nearest neighbour method relies on calculating the distance from one galaxy to another. I shall therefore begin by showing how to do this. Given a galaxy's right ascension (ra), declination (dec) and redshift, one can in principle calculate the galaxy's position within the (three dimensional) sphere that is centred on the Earth. The ra and dec correspond directly to the azimuth and altitude angles respectively used in spherical polar geometry. Before deriving the distance to another galaxy, I first need to derive the relation between the scale factor a and redshift z, namely that a is proportional to $1/(1+z)$.

The scale factor is defined by the equation

$$\mathbf{r} = a(t)\mathbf{x} \tag{3.1}$$

where $\mathbf{r}$ is the real distance between two objects and $\mathbf{x}$ is the comoving distance between the objects. Hubble's Law can thus be rewritten as:

$$\mathbf{v} = \frac{|\dot{\mathbf{r}}|}{|\mathbf{r}|}\mathbf{r} \tag{3.2}$$

Then substituting in equation 3.1 yields:

$$\mathbf{v} = \frac{\dot{a}}{a}\mathbf{r} = H\mathbf{r} \tag{3.3}$$

where the second equation is the form of Hubble's Law stated in equation 1.2. It immediately follows that

$$H = \frac{\dot{a}}{a} \tag{3.4}$$

Now consider two objects that are close together. One object emits a photon that travels to the other object. From equation 1.1, it follows that

$$\frac{v}{c} = \frac{\lambda_o}{\lambda_e} - 1 \tag{3.5}$$

Differentiating v with respect to λ_o gives:

$$\frac{dv}{d\lambda_o} = \frac{c}{\lambda_e} = \frac{c}{\lambda_o}\frac{\lambda_o}{\lambda_e} \tag{3.6}$$

Now, given that the objects are close together and thus that, from Hubble's Law, v << c, it follows that

$$\frac{dv}{c} = \frac{d\lambda_o}{\lambda_o} \tag{3.7}$$

We next differentiate v with respect to r in equation 3.4 (again assuming the two objects are close) and substitute this into equation 3.7 to give:

$$\frac{d\lambda_o}{\lambda_o} = \frac{\dot{a}}{a}dt = \frac{da}{a} \tag{3.8}$$

On integrating equation 3.8, we get

$$\lambda_o \propto a \tag{3.9}$$

and thus

$$\frac{\lambda_o}{\lambda_e} = \frac{a_o}{a_e} = z + 1 \tag{3.10}$$

Then setting $a_o = 1$ (i.e. normalise the scale factor to the present day value) yields:

$$a = \frac{1}{1+z} \tag{3.11}$$

It will also be useful to differentiate a with respect to z to give:

$$\frac{da}{dz} = -a^2 \tag{3.12}$$

We are now ready to convert redshift to radial (comoving) distance. Start with the Robertson-Walker metric,

$$ds^2 = c^2dt^2 - a^2\left[\frac{dr^2}{1-kr^2} + r^2(d\theta^2 + sin^2 d\phi^2)\right] \tag{3.13}$$

where s is the spacetime interval between two events (in this case, the emission and detection of a photon), c is the speed of light, t is time, a is the expansion parameter, r is the radial distance to the galaxy, k is the flatness parameter, θ is the declination of the galaxy and ϕ is the right ascension of the galaxy.

For a given galaxy, it is always possible to choose the coordinate axes such that $d\theta = d\phi = 0$. In the ΛCDM cosmology described above, I am taking $k = 0$ too. Remembering that $ds = 0$ for a photon and integrating yields:

$$r = c\int \frac{1}{a}dt \tag{3.14}$$

Therefore

$$r = c\int \frac{1}{a}\frac{dt}{da}da \tag{3.15}$$

Then substituting in $H = \dot{a}/a$ yields:

$$r = c\int \frac{1}{H}\frac{1}{a^2}da \tag{3.16}$$

Substituting equation 3.12 into equation 3.16 gives:

$$r = -c \int \frac{1}{H} dz \tag{3.17}$$

Thus, we now just need to see how H evolves with z in order to get the distance to the galaxy from its redshift. In order to do this, consider again the Friedmann equation:

$$H^2 = \left(\frac{\dot{a}}{a}\right)^2 = \frac{8\pi G}{3}\rho + \frac{\Lambda}{3} - \frac{k}{a^2} \tag{3.18}$$

We need to rewrite this equation in terms of the critical density. Remembering that, since ρ is proportional to a^{-3},

$$\frac{\rho}{\rho_c} = \frac{\rho_0}{\rho_c}\frac{1}{a^3} \tag{3.19}$$

yields from equation 3.18:

$$\left(\frac{H}{H_0}\right)^2 = \frac{\Omega_M}{a^3} - \frac{k}{H_0^2 a^2} + \Omega_\Lambda \tag{3.20}$$

Now, rewriting equation 3.18 for the present epoch gives:

$$H_o^2 = \frac{8\pi G}{3} - \frac{k}{H_0^2 a^2} + \frac{\Lambda}{3} \tag{3.21}$$

Dividing this equation through by H_0^2, re-arranging, substituting into equation 3.20 and re-arranging again gives:

$$H = H_0\left[(1+z)^2(1+\Omega_M z) - \Omega_\Lambda z(2+z)\right]^{1/2} \tag{3.22}$$

Thus, for given values of Ω_M and Ω_Λ, equations 3.17 and 3.22 between them give the numerical integration to derive the distance to a galaxy given its redshift. With this information, it is easy to calculate the difference in radial distances between two galaxies. In order to calculate the angular size distance between two galaxies (i.e. the projected separation on the sky), consider again the Robertson-Walker metric in equation 3.13. Consider the two galaxies both to be distance r from the Earth and subtending an angle $\Delta\psi$ at the Earth. They are distance s ($=\int$ ds) apart from each other. Since the two events now are the emission of two photons, one from each of the galaxies simultaneously, dt = 0. We again choose k = dϕ = 0 and dθ = dψ. Simplifying the metric this time gives:

$$ds = ard\theta \tag{3.23}$$

where r is simply the distance to either galaxy, as calculated using equations 3.17 and 3.22. Finally, substituting in the relationship between a and z and integrating gives:

$$s = \frac{1}{1+z} r\Delta\theta \tag{3.24}$$

To calculate the angle $\Delta\psi$ from the ra and dec, use the following equation derived from spherical polar coordinates:

$$\Delta\psi = cos^{-1}\left[cos\theta_1 cos\phi_1 cos\theta_2 cos\phi_2 + cos\theta_1 sin\phi_1 cos\theta_2 sin\phi_2 + sin\theta_1 sin\theta_2\right] \tag{3.25}$$

where ϕ_i and θ_i are the ra and dec of the i^{th} galaxy respectively.

The n^{th} Nearest Neighbour Density Estimate

Finally, we are in a position to calculate the distance from one galaxy to another: we simply add the difference in the two galaxies' comoving radial distances (crd) from Earth to their projected separation in quadrature. The method of n^{th} nearest neighbour density calculation usually involves counting the number of galaxies in either a circle or a sphere. If the distance to the n^{th} nearest galaxy is d, a 3 dimensional, spherical density ρ would be calculated as

$$\rho = \frac{n}{\frac{4}{3}\pi d^3} \tag{3.26}$$

However, a 2 dimensional, circular density Σ would be calculated as:

$$\Sigma = \frac{n}{\pi d^2} \tag{3.27}$$

The choice of which density to use is a difficult one. The above analysis assumed that redshift information is available and assuming that, in reality, the galaxies do live in a three dimensional space, the three dimensional density would obviously be preferable if it were possible.

The major problem with this method is due to galaxies' peculiar velocities. Consider two high redshift galaxies that are very close together. They both have a receding

velocity from Earth due to the Hubble flow but, in addition, one of them also has a very large velocity relative to the other one. This may be, for example, due to its position in an orbit around the core of a dense cluster and is called the galaxy's peculiar velocity. Since the distances to these galaxies are being calculated from their redshifts which in turn depend on the galaxies' velocities, one will infer a large separation between them when in fact their separation is small. This effect has particularly difficult ramifications for deriving densities in regions containing large peculiar velocities (e.g. centres of clusters of galaxies) and also on smaller scales where the radial separations are smaller. The smaller scales issue is particularly prevalent in surveys that are not very deep because the comoving radial separations (crs) are smaller and for low redshift galaxy surveys in general because, as I show later in this work, the average galaxy's environmental density has increased with cosmic time. [29] found that even redshift errors of $\sigma_z = 0.02$ smear out line-of-sight galaxy distributions on small scales (rendering any photometric redshifts unequal to the task). Thus, the two dimensional density is often used when studying the densities of galaxies in groups and clusters. However, even when a 2 dimensional, projected density is to be used, radial information can still be usefully incorporated into the calculation. For example, when B04 calculated their projected densities, they only measured distances to galaxies that had been pre-selected as being within $\pm$ 1000kms^{-1} of the galaxy whose environmental density was being measured. In this way, they excluded any galaxies that, although close to the line of sight of the galaxy in question, were actually just foreground or background objects that didn't affect the galaxy's environment at all.

A further decision to be made is the value of n. Choosing a very low value of n, such as 1 or 2, risks implying a very "noisy" density distribution. This is because, for example, if a galaxy is a long way from all other galaxies except one, measuring its density by using its distance to the first nearest neighbour will greatly overestimate the density. If too large a value of n is chosen, e.g. $n > 5$, then the density could be overestimated or underestimated because one will likely be using the distance to the next structure (e.g. the next group of galaxies). Thus all galaxies would be assigned a very similar environmental density. [29] found that the densities were relatively (e.g. compared to problems from peculiar velocities) insensitive to the value of n if n was chosen to be 2, 3 or 5. These values corresponded to the sizes of small groups detected in the DEEP2

survey.

3.1.2 Number of Counts in an Aperture

Another, much simpler, method of measuring density is to simply count the number of galaxies within a fixed metric aperture, for example a sphere, of known radius centred on the galaxy whose redshift has been determined spectroscopically and whose density is to be measured. It is assumed that only some of the galaxies in the field of view are suitable for deriving spectroscopic redshifts and that the others are simply counted because only photometric redshifts are available. However, this method is likely to produce a noisy density because the count is likely to include foreground and background galaxies and thus overestimate the density. This is because galaxies whose redshifts are only determined photometrically may be included in the count (i.e. subtracting the background is a very uncertain procedure). The main problem with this method is that, for high redshift galaxy surveys where the area on the sky that is covered may be of the order of 1 $\square^0$, larger apertures will be more affected by the edges of the survey. For example, within a 30" $\times$ 30" field (i.e. 20 h^{-1} comoving Mpc on a side at z $\sim$ 1), 81% of circular apertures with a radius of 1 h^{-1} comoving Mpc will fit within the surveyed field. However, for apertures of radius 3 h^{-1} and 5 h^{-1} comoving Mpc, only 49% and 25% respectively of the field will be unaffected by the edges of the survey. It is not believed that larger apertures provide any advantage or additional information worth the price. In addition, they will be measuring over scales that are less relevant to the galaxy.

The aperture count method does have one advantage to it. Since it is less susceptible to redshift space distortion (rsd) by definition (than, for example, the n^{th} nearest neighbour method), along with *projected* n^{th} nearest neighbour density, it is better suited to calculating the densities in more dense regions such as cluster centres. The 3-dimensional n^{th} nearest neighbour distance and the Voronoi method, described below, on the other hand, are more suited to working in less dense regions.

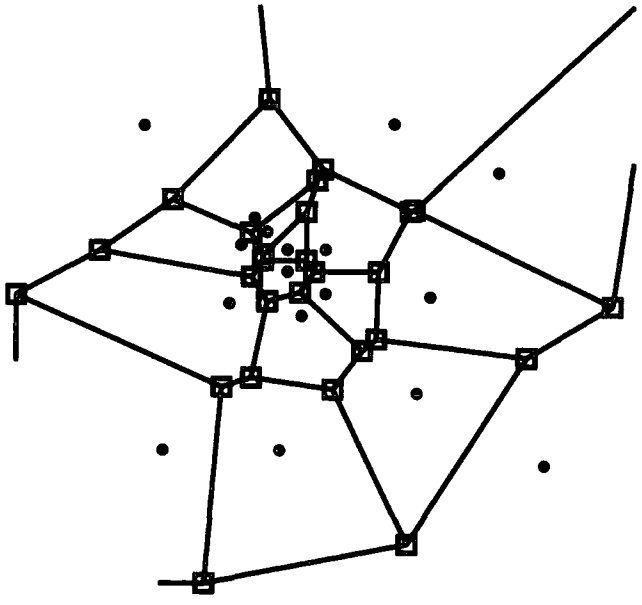

Figure 3.1: Demonstration of Voronoi Volumes around galaxies [29]

3.1.3 Voronoi Volume

A third method for calculating a galaxy's density is to use a " Voronoi Volume". As in figure 3.1, each galaxy has a Voronoi volume around it defined as a unique polyhedron enclosing a three dimensional space, every point of which is closer to the galaxy in question than to any other galaxy. [60] provides computational details and further discussion of the usefulness of the Voronoi method. It is worth reporting here [29]'s results from a comparison of the Voronoi volume and n^{th} nearest neighbour volume in a DEEP2-selected mock field of 120' $\times$ 30'. Figure 3.2 plots the cube of the distance to the 5^{th} nearest neighbour versus the Voronoi volume for galaxies not within 5 h^{-1} comoving Mpc of an edge of the survey. The strong agreement between these two volume estimators is quantified by a Spearman ranked coefficient of 0.85. However, [29] also found that, for the simulated DEEP2 data, the n^{th} nearest neighbour distance was much more robust to edge effects than was the Voronoi method. Given that the n^{th} nearest neighbour distance is also much cheaper computationally, I chose it over the Voronoi method when carrying out the present work.

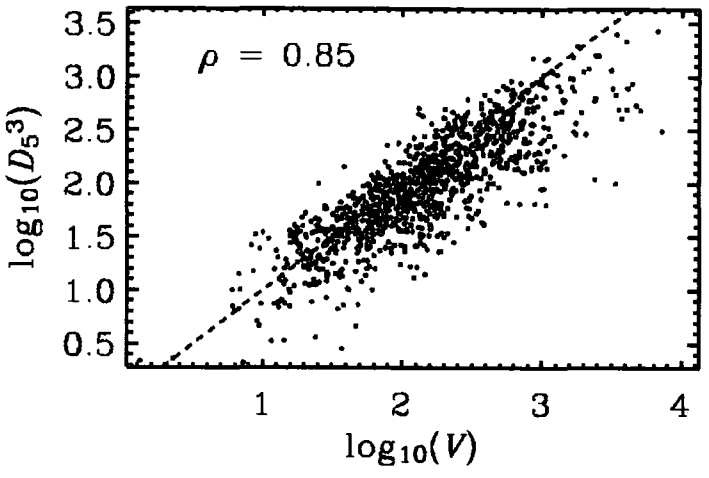

Figure 3.2: Plot of the cube of the 5^{th} nearest neighbour distance versus vs the Voronoi volume. The galaxies plotted are only those that are not within 5 h^{-1} comoving Mpc of an edge of the survey. The strong agreement between the two is quantified by the Spearman ranked correlation coefficient of 0.85
[29]

3.2 Measuring Environmental Density in the Groth Strip Volume Limited Sample

In measuring the density of the environment in the Groth Strip, I elected to employ the 3-dimensional n^{th} nearest neighbour method with a correction for peculiar velocities that is described below. The method of counting galaxies in an aperture would not be suitable to this high redshift survey whose area on the sky is a very elongated 40' × 5'. As described above, the Voronoi volume correlates well with the 3-d n^{th} nearest neighbour method. As a final comparison between these two methods, [29] analysed the effect of redshift space distortion (rsd) on each volume method. They defined the percent change in environment measure X for galaxy q, $\Delta_z(X)$ as:

$$\Delta_z(X) = \frac{log_{10}(X_{z,q}) - log_{10}(X_{R,q})}{\sigma_R} 100\% \tag{3.28}$$

where $X_{z,q}$ is the measure of X for galaxy q computed from the redshift-derived position, $X_{R,q}$ is the measure of X similarly computed from the real-space position in the mock DEEP2-selected spectroscopic catalogue and σ_R is determined via a Gaussian fit to the logarithmic distribution of environment measure X for all galaxies in the real space

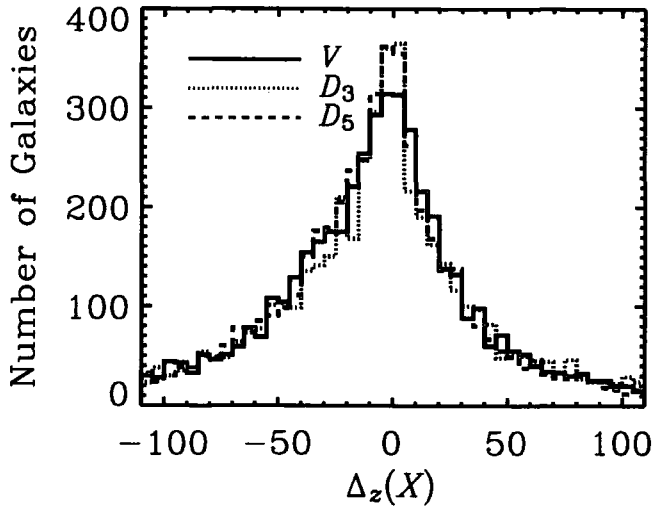

Figure 3.3: The effects of redshift space distortion on each of the Voronoi method and the 3-dimensional n^{th} nearest neighbour method for n=3, 5. Δ_z(X) is defined in equation 3.28 and is plotted here for 5,031 galaxies in the DEEP2-selected simulation within $0.7 < z < 1.4$ and more than 4 h^{-1} comoving Mpc from any survey edge [29]

simulation. The histogram of Δ_z(X) is shown in figure 3.3. It is immediately clear from this histogram that the two measures are affected very similarly by rsd and thus neither gains an advantage on this score.

So, owing to the smaller computation requirements and greater robustness to edge effects, the 3-d n^{th} nearest neighbour method was chosen.

The issue of peculiar velocities still had to be dealt with, however. In order to counter this problem, I set to zero any comoving radial separation (crs) that could have been inferred purely from a peculiar velocity of 300kms^{-1} (approximately a typical peculiar velocity of a galaxy in a group) and took the projected separation to be the total separation. The method is thus the fully fledged 3-dimensional n^{th} nearest neighbour method for galaxies in lower density environments and the projected n^{th} nearest neighbour method for galaxies in the densest environments, thus utilising the best methods, as described above, in both types of environment.

In order to quantify the uncertainty in redshift z due to a peculiar velocity v, consider the following relationships which are derived from equations 1.1 and 3.16:

$$\delta z \sim \frac{H}{c}\delta r \tag{3.29}$$

$$\delta z \sim \frac{1}{c}\delta v \tag{3.30}$$

$$\delta r \sim \frac{1}{H}\delta v \tag{3.31}$$

where H is measured in $kms^{-1}Mpc^{-1}$, c=3x10^5 kms^{-1}, r is measured in comoving Mpc and v is measured in kms^{-1}.

Equation 3.30 shows that an uncertainty in v of 300kms^{-1} (it would be 1000kms^{-1} for a deep cluster environment) translates to an uncertainty in z of 0.001 (0.003). This uncertainty in z due to peculiar velocity is independent of the size of z and thus has a greater effect at lower z. Thus B04 opted for the "quasi two dimensional density" alluded to above. They considered galaxies that were within ±1000kms^{-1} of the galaxy in question but, in actually computing the density, only considered the projected separations. (B04 also only considered galaxies brighter than M_r = -20 necessitating a correction to my data for them to be compared to those of B04, as described in section 3.6). Working at higher z and with bigger crs, I decided to accept a crs that couldn't have been inferred from a peculiar velocity of 300kms^{-1} as genuine and used it to form a three dimensional density. I considered galaxies that were within 35Mpc (in any direction) and 0.01 radians of the galaxy in question. These values were chosen so as to include all galaxies that could possibly affect the environment of the galaxy under study without including those too far away to do so. Histograms of the crs, angular separations and total separations, together with a histogram of the galaxies' redshifts, are shown in figure 3.4.

Galaxies whose 5th nearest neighbour was more than 35Mpc away were given a nominal density of 1x10^{-5} galaxies Mpc^{-3}. This corresponds to $r_5 \sim$ 50Mpc.

3.2.1 Survey Edges

A further complication was the geometry of the survey. As can be seen from figure 2.1, the area on the sky is very long and thin. Additionally, given the large redshifts of the

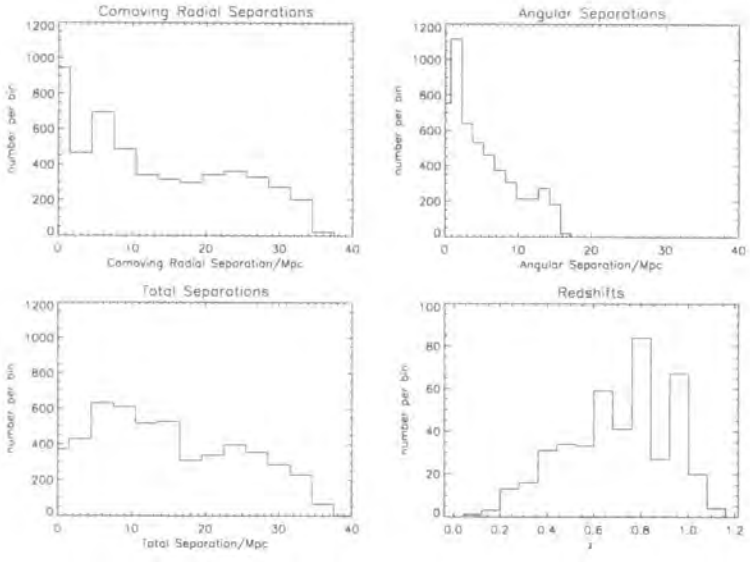

Figure 3.4: The Groth Strip Galaxies: histograms of (top left panel) the comoving radial separations (crs), (top right panel) the angular separations, (bottom left panel) the total separations, (bottom right panel) the galaxies' redshifts. The peak at the smallest angular separation is real but the peak at the smallest comoving radial separation is not. This peak is due to all crs that could have been inferred from a peculiar velocity of only 300 kms^{-1} being set to zero (see text).

galaxies in the survey, the survey's radial dimension is thousands of times its projected dimension. This means that all bar 4 of the 433 galaxies were closer to a survey edge than they were to their 5th nearest neighbour. We have no way of knowing the density of galaxies in the space outside the survey and thus, if densities are made using only those galaxies in the survey, an "edge correction" to the densities was needed.

This was done by calculating the distance from each galaxy to each "wall" of the survey. I assumed that the projection of the survey volume onto the sky could be approximated by a rectangle. Then, for up to 2 walls that were closer to the galaxy than the 5th nearest neighbour, the correction was made as follows. Since the wall was effectively a plane intersecting a sphere (of radius r_5), the volume of the sphere that was on the side of the plane outside the survey was simply removed and the density recalculated accordingly. Figure 3.5 shows the situation schematically. To have used more than two walls would have introduced further complications regarding volumes being removed more than once.

The average percentage change in the galaxies' densities due to the correction for the

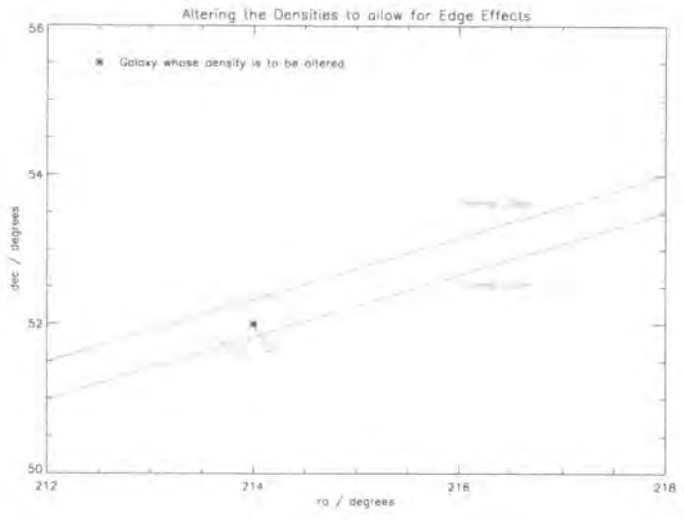

Figure 3.5: Allowing for the edge effects. The distance to the 5^{th} nearest neighbour (r_5) of the galaxy whose density is being measured extends either side of the narrow survey area. The ellipse denotes the projection of a slice through the sphere of radius r_5. The volume of the sphere that is outside the survey must be removed before that volume can be used to calculate a density.

edge effects was 75%. This very large figure reflects the problem of the geometry of this survey.

Finally, the galaxies, along with their U-B colours, were spread in equal numbers between 5 bins of increasing environmental density. The number of 5 bins was chosen as a compromise between higher numbers which would have facilitated the inference of any trends in U-B colour as a function of environmental density and lower numbers which would have increased the signal to noise ratio.

3.3 Fitting the Double Gaussians

Figure 3.6 shows the 5 histograms (one for each density bin) of the galaxies' U-B colours. The density increases from left to right across the histograms. The error bars on the histogram columns are simply the square root of the value of the column. It is immediately apparent that the colour distributions are bimodal (blues on the left in each histogram, reds on the right) and thus suitable for fitting with a double Gaussian function. A double Gaussian is simply the sum of two Gaussian functions:

$$y = A_1 e^{-(x-x_1)^2/w_1^2} + A_2 e^{-(x-x_2)^2/w_2^2} \tag{3.32}$$

There are thus a maximum of 6 free parameters, namely the amplitude (A_i), centre (x_i) and width (w_i) of each of the two distributions. Initially, only the two widths were fixed with the other 4 parameters being free. The widths were fixed at the widths of the red and blue distributions in the colour distribution of all 433 galaxies (i.e. all 5 histograms combined). These widths were 0.255 magnitudes for the blue distribution and 0.162 magnitudes for the red distribution. Then the iterative *curvefit* procedure in Interactive Data Language (IDL) fitted the double Gaussian to the data, taking the middles of the tops of the bars in the histogram to be the data points. The double Gaussians were fitted by finding the values of the other 4 parameters that minimised χ^2.

At this point, the first result was found. Namely that the colours of each distribution varied very little with environmental density. That is, the centres of the red distributions were almost identical in all 5 histograms and similarly for the blues. This result is shown graphically in figure 3.7 which plots the mean colours of the red and blue distributions versus density and shows a comparison with the corresponding results from B04. This remarkable result, with ramifications for star formation rates and the evolution of galaxy colours, is mentioned only briefly here in order to explain the way the analysis was carried out hereafter. It is discussed more in chapter 5. Note that, in figure 3.7, the U-B colours from the Groth Strip galaxies have been transformed to the u'-r' colours used in the SDSS. This process is explained in section 3.5 and is done via two different methods, as shown in the figure. Throughout this report, I shall denote wavebands used in the SDSS photometric system with apostrophes (e.g. u'-r').

Given that the centres of the distributions were changing so little, in order to further reduce the number of free parameters (and thus test the applicability of the fitting of the double Gaussian more robustly), the centres of each colour distribution were then fixed. In each of the 5 histograms they took the values of -0.185 for the red distribution and 0.33 for the blue distribution hereafter. Now the only free parameters were the 2 amplitudes of the distributions. Figure 3.6 shows each of the 5 histograms, the fitted double Gaussian and the value of χ^2 in each histogram.

Histogram	n	χ^2	p(χ^2 | n)
1	9	14.0	0.12
2	8	5.9	0.66
3	8	3.4	0.91
4	8	0.7	1.00
5	9	8.0	0.53

Table 3.1: The values of n, χ^2 and the probability of getting at least that χ^2 given n for each of the 5 histograms in figure 3.6

The values of χ^2 in the histograms of figure 3.6 merit further discussion. For a function to be well fitted to a set of points, the value of χ^2 should be as close to n, the number of degrees of freedom (defined as the number of points to be fitted minus the number of free parameters) as possible. If χ^2 is much larger than n then the function is simply inappropriate for the data points and a new one must be sought. If it is much smaller then the natural scatter of the points would cause suspicion that there are too many free parameters (within reason, *almost any* function could be well fitted to a set of data points if there are enough free parameters). Table 3.1 summarises the results of this analysis. The histogram numbers refer to the histograms in figure 3.6 (i.e. histogram 1 is the least dense, 5 is the densest). The probabilities in the 4^{th} column are the probabilities of getting a value of χ^2 greater than or equal to the value of χ^2 in the 3^{rd} column given the number of degrees of freedom in the 2^{nd} column.

Thus the value of χ^2 in the left most histogram is larger than hoped for. The first reason for this, as can be seen in figure 3.7, is that the colour of the red distribution in this histogram isn't quite as red as the other 4 which are almost identical. Thus, when the colour was fixed at that of the other 4 histograms, the fit in the left most histogram would always be worse. It is also likely that, as the histogram containing the galaxies in the least dense environments, it is also the one that is most contaminated by edge effects. It is the only histogram in which the trend line misses the red population; perhaps the peak was too narrow for the model. The other values of χ^2, apart from that for the 4^{th} histogram, are thus of the right order. The χ^2 value in the 4^{th} histogram is very small but, since the same method has been used for the others, I put this down to a fortuitously good fit!

3.4 The Ratio of Galaxies that are red

The next step was to find the ratio of red galaxies to the total number of galaxies for each density bin. To this end, the above approach was slightly modified. The two amplitudes were re-parameterised as the amplitude of the blue population and the ratio of the amplitude of the red population to that of the blue distribution. The benefit of this technique was that, in calculating the ratio of red galaxies to all galaxies as $A_r w_r/(A_r w_r + A_b w_b)$, the error in this ratio would only come from the error in one parameter in the χ^2 minimisation, namely the ratio of amplitudes. The error in this parameter was defined as the amount by which the value would need to be changed from the value that minimised χ^2 to the value that raised the reduced χ^2 (that is χ^2 divided by the number of free parameters) to the reduced χ^2 +1. Statistically, this error corresponds to a 1σ limit. For details, see [9] . Figure 3.8 shows how the ratio of red galaxies to all galaxies changes with environmental density. The error bars on this plot are those derived from the process above. The equivalent plot from B04, using the SDSS first data release, is plotted alongside for comparison. I shall discuss these results in chapter 4 and their implications in chapter 5

3.5 Colour Conversions between different Photometric Systems

As described above, figure 3.7 shows how little the mean colours of the red and blue distributions vary with density and the equivalent result from B04 who carried out a similar analysis on galaxies in the local universe. Apart from the fact that the colours of all four distributions (red and blue in the high and low redshift universes) vary little with density, it is also interesting to note the changes in the mean colours between the epochs. This change is analysed formally in section 4.4 but it is necessary to first describe how the Groth Strip galaxies' U-B colours in the Johnson magnitude system were converted to u'-r' colours in the SDSS photometric system.

For comparative purposes, I did this conversion two ways. The first was to use the conversion equations of Fukugita [38]. By observing stars with known U, B and V

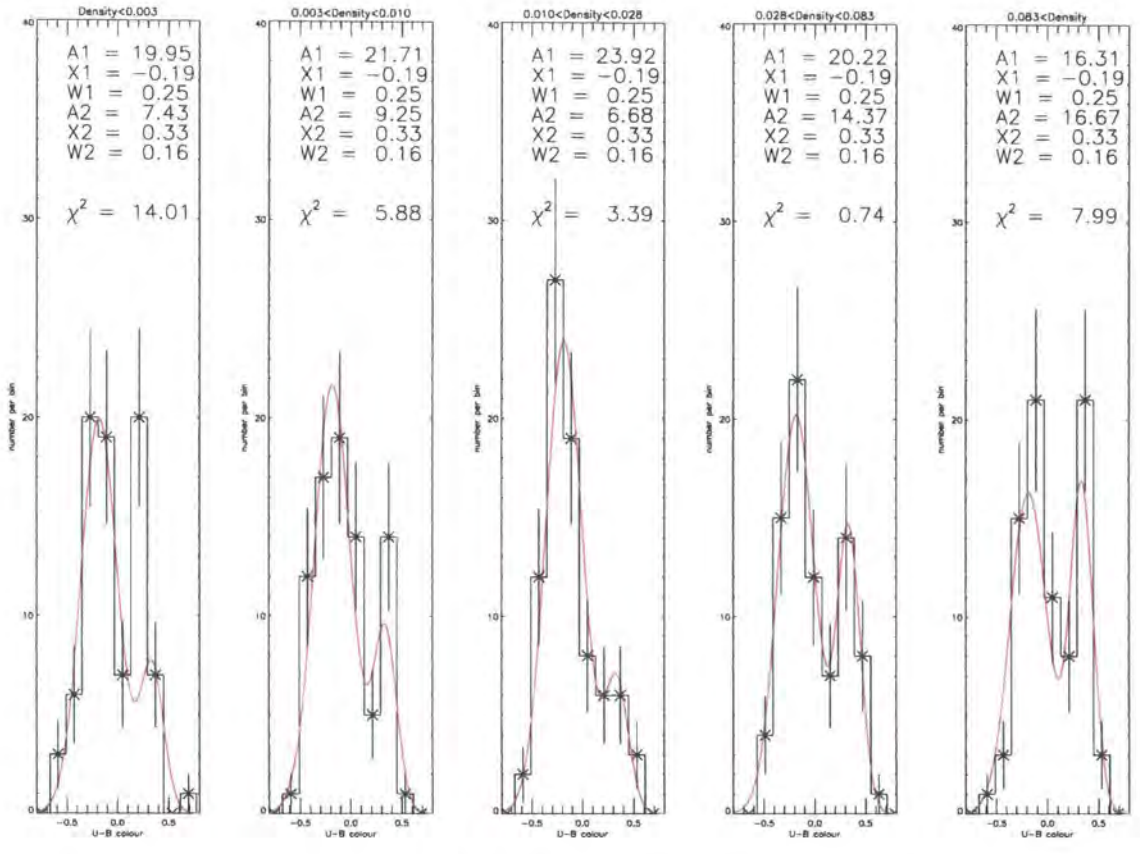

Figure 3.6: Histograms of the Groth Strip galaxies' U-B colours. Each histogram contains galaxies within a particular density range. The left most histogram contains the galaxies in the least dense environments, the right most contains galaxies in the most dense environments. The errors on the bars are simply the square roots of the bar heights.

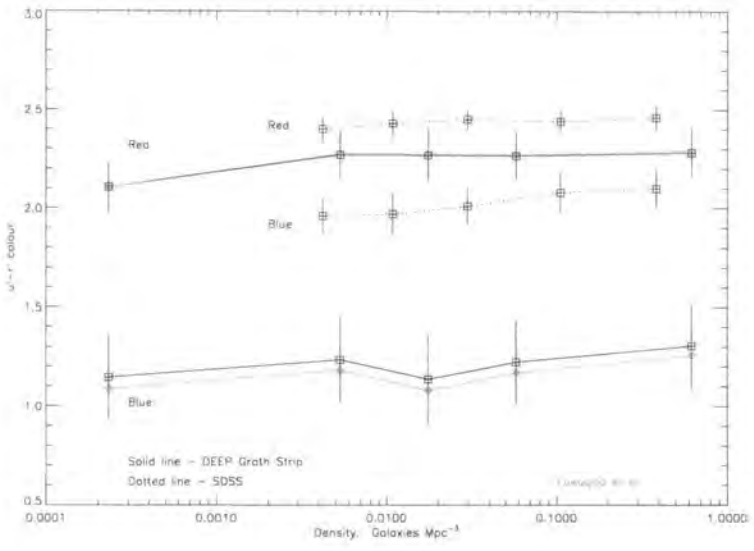

Figure 3.7: The mean u'-r' colours of the red and blue distributions of galaxies from both the Groth Strip and from the SDSS. For comparative purposes, the conversion of the Groth Strip Galaxies' U-B colours into u'-r' was done via two sets of conversion tables, namely those of Fukugita et al [38] and of Krisciunas & Tonry [56]. Hence the two lines for each of the red and blue distributions of the Groth Strip galaxies

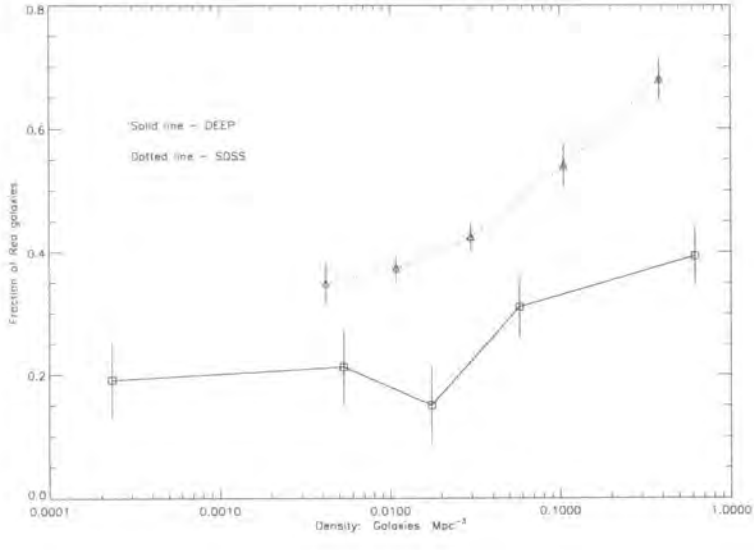

Figure 3.8: The fraction of red galaxies to the total number of galaxies as a function of environmental density for galaxies in the Groth Strip and for those in the SDSS

magnitudes with the Sloan filters, Fukugita et al. derived the following relations:

$$u' - g' = 1.38(U - B) + 1.14 \tag{3.33}$$

and

$$g' - r' = 1.05(B - V) - 0.23 \tag{3.34}$$

Combining equations 3.33 and 3.34 yields:

$$u' - r' = 1.38(U - B) + 1.05(B - V) + 0.91 \tag{3.35}$$

Thus, it was necessary to convert the U-B colours into B-V colours. This was done using the lines corresponding to z=0 of tables containing no evolution colours (one U-B table and one B-V table) of galaxies of different types, from E/S0 to Sdm. Using first the U-B table, the U-B colour of the galaxy in question was used to find that galaxy's "position" in the z=0 line (i.e. what type of galaxy it is). It was then assumed to hold the same position in the z=0 line in the B-V table and its B-V colour was read off accordingly. I was then able to convert the Groth Strip galaxies' colours to those of the Sloan Photometric System to compare them to those of galaxies in the local universe obtained by B04.

The second set of equations, used to check the conversion of Fukugita et al, was that of Krisciunas & Tonry [56]:

$$u' - g' = 1.3290(U - B) + 1.1786 \tag{3.36}$$

and

$$g' - r' = 0.9578(B - V) - 0.1803 \tag{3.37}$$

Then equations 3.36 and 3.37 together yield:

$$u' - r' = 1.3290(U - B) + 0.9578(B - V) + 0.9983 \tag{3.38}$$

3.6 Density Corrections

To validate the comparison between the densities in the two surveys, two further corrections were required. Firstly, the magnitude limit of the SDSS (r' = -20.0) corresponded to a B limit of -19.28 (conversion done using [56]). This is different to the limit of B = -19.0 that I had chosen for my volume limited sample. Thus, the SDSS was sampling over a smaller brightness range of galaxies. The correction factor, by which the Groth Strip galaxies' densities were to be divided, was calculated as the ratio of the number of galaxies brighter than -19.0 to the number of galaxies brighter than -19.28. These numbers were calculated by integrating the Schechter Luminosity Function:

$$Ratio = \frac{\int_{-\infty}^{-19.0} \phi(M) dM}{\int_{-\infty}^{-19.28} \phi(M) dM} \tag{3.39}$$

where ϕ(M) dM is given by equation 1.12. The ratio was calculated to be 1.065

The second correction was to account for the fact that the SDSS density was a two dimensional one whereas the Groth Strip one was three dimensional. This correction was made by dividing the SDSS densities by (2000/H). The 2000 comes from twice the 1000kms^{-1} used in B04. H is Hubble's constant. This factor comes from equation 3.31.

Of course, all the colour conversions and density corrections described in this and the previous sections introduce their own intrinsic uncertainties into the calculations. A preferable method and possibility for future work, from the point of view of comparing my work to that of B04, would be to carry out my analysis on the Sloan data.

Chapter 4

Results

In this chapter I present my results from the analysis of the Groth Strip galaxies. The results are shown graphically in figures 3.6 (histograms of the galaxies' U-B colours binned according to environmental density), figure 3.7 that shows how (little) the mean colours of the red and blue distributions change with environmental density and figure 3.8 that shows how the fraction of galaxies that are red changes with environmental density. Section 4.1 discusses these plots and states all of my results. The latter two of these three figures include the equivalent results from B04 in the local universe. This inclusion permits a comparison of the two epochs and an analysis of the evolution of galaxy colours. The two epochs are compared in section 4.2 and the evolution of galaxy colours is discussed in section 4.3. Then, in section 4.4, I present an analysis of this colour change, asking what is responsible for the change in the mean colour of galaxies between $z \sim 1$ and $z \sim 0$.

4.1 My Results

My first result is that the distribution of colours of the Groth Strip galaxies is well fitted by the sum of two Gaussian functions (a "double Gaussian"). This is at least true where the edge effects permit a reliable density measurement and where the mean colours of the red and blue populations are close to the fixed values. As explained in section 3.3, it is for these reasons that the fit in the leftmost histogram in figure 3.6 is poor. As shown in figure 3.6, the values of χ^2 are, on the whole, of the right order in 5 bins selected according to the galaxies' environmental density.

My most important result is that the fraction of Groth Strip galaxies that lie in the red distribution increases with the density of the galaxies' environment. The fraction increases from ~ 0.2 to ~ 0.4 whilst the environmental density increases from $\sim 2\times10^{-4}$ galaxies Mpc^{-3} to $\sim 4\times10^{-1}$ galaxies Mpc^{-3}. This is shown in figure 3.8. Although this result is not unexpected, it is still interesting to note that, even by this time (approximately 5Gyr after the Big Bang), a galaxy's colour was correlated with the environment in which the galaxy was sited. Various possible reasons for this are discussed in the latter sections of this chapter and in the next chapter.

Finally, the mean colours of the red and blue distributions vary very little with the density of the galaxies' environment. In fact, above a density of 4×10^{-3} galaxies Mpc^{-3}, the mean colour of the red distribution varies imperceptibly from (u'-r') ~ 2.25. The mean colour of the blue distribution is more scattered, around (u'-r') ~ 1.2. These results are shown in figure 3.7.

4.2 Comparison of the two Epochs

Figures 3.6, 3.7 and 3.8 are the high redshift equivalent figures of figures 1.12, 1.13 and 1.14 respectively. Notice that in figures 1.13 and 1.14 the galaxies have also been split into different luminosity bins. The luminosity bin equivalent to the Groth Strip galaxies is $-22 < M_r < -21$.

Figure 3.6 immediately confirms the bimodal distribution of the colours of the galaxies in the Groth Strip. This confirms the result of [6]. The immediate questions to ask are, "What causes colour bi-modality at this redshift?" and "Are the causes the same as those at low redshift?" I shall attempt to answer these questions in chapter 5.

The increase in the fraction of galaxies that are red is found both at high redshift and in the local universe. However, it is also clear that the strength of the trend is greater in the local universe. Therefore, it is possible that, whatever is causing the increase, it is more pertinent in the local universe. Alternatively, if this result is due to more than one effect, perhaps one or more of those effects are only low redshift phenomena. Again, these interpretations are discussed in chapter 5.

The difference between the two fractions increases with density and is greatest in the

densest environment, presumably those of the cluster centres. This means that there are more blue galaxies in cluster centres at high redshift than there are today and this is evidence of the Butcher-Oemler Effect. This effect was first reported in 1978 by [14]. Further, the average density of a galaxy's environment is higher in the local universe than it was at z $\sim$ 1. This is consistent with the idea of galaxies falling into the potential wells of clusters with cosmic time.

The mean colours of the red and blue distributions of local universe galaxies were also found to vary very little with environmental density. The red colour again varied less than the blue, differing little from (u'-r') $\sim$ 2.45. The blue colour was (u'-r') $\sim$ 2.0 although their error bars are small enough to hint at a very weak trend of the colour getting redder with environmental density. Whether this weak trend is also there at high redshift is impossible to discern given the size of the error bars. These results have been seen before in the local universe - it is especially true that the properties of early type galaxies are nearly independent of density (e.g. early type galaxies: [7], late type galaxies: [58]).

4.3 The Evolution of Galaxy Colours

Additionally, both red and blue distributions are bluer than those at low redshift. Between the two epochs, the red distribution colour becomes redder by $\sim$ 0.2 magnitudes and the blue distribution becomes redder by $\sim$ 0.8 magnitudes. In order to test whether these colours could be explained by "isolated evolution", I used the PÉGASÉ software to investigate whether a galaxy could evolve with an exponentially decaying star formation rate. To clarify terms, by "isolated evolution", I refer to a galaxy evolving without any external influences on its star formation or morphology. The star formation rate in PÉGASÉ is parameterised as:

$$SFR = \frac{A}{B} e^{-t/B} \tag{4.1}$$

where A is measured in $M_\odot$ and B in Myr. I could not find a pair of values for A and B that would produce the right colours at the right times, either for the red distribution or the blue one. Figure 4.1 shows plots of u'-r' colours versus age of the universe for

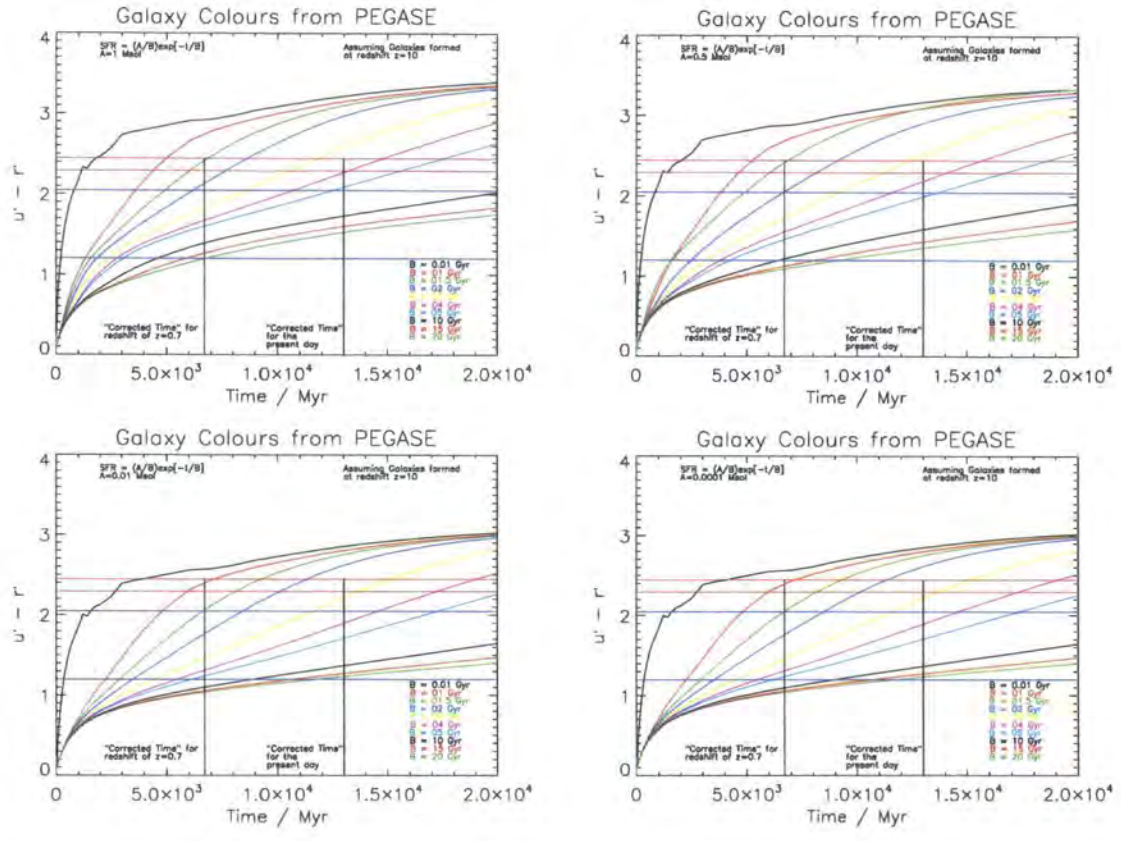

Figure 4.1: The evolution of galaxy u'-r' colours according to the PÉGASÉ software. Using the parameterisation defined in equation 4.1, A=1M⊙ (top left panel), 0.5M⊙ (top right panel), 0.01M⊙ (bottom left panel) and 0.0001M⊙ (bottom right panel). The red and blue horizontal lines show the mean colours from figure 3.7. The vertical black lines show the points in time at which the two sets of data in figure 3.7 are observed. Note that, since I am making the assumption that the galaxies formed at z=10 in this plot, these vertical black lines have been shifted left by the age of the universe at z=10. Thus, for a particular evolutionary track to be consistent with both sets of results for the blue galaxies, it must intersect the bottom left and top right hand corners of the rectangle formed by the two vertical black lines and the two horizontal blue lines and similarly for the red galaxies. It is clear that no track will provide an accurate match for either the red galaxies or the blue ones.

different values of A and B. The values of A and B are shown on the panels and the caption explains the other lines on the panels. The gap in the colours of the blue distribution at the two epochs was too great to be produced by this method. Similarly, the gap in the red distribution's colours was too small. It is, however, perhaps more surprising that the difference in the red colours cannot be reproduced by P*ÉGASÉ* and this would be a suitable line of further enquiry. These results are consistent with the blue galaxies being disrupted by external influences (that is, influences in all types of environment), having their star formation quenched or stopped and then joining the red distribution. These results are discussed in full in chapter 5.

4.4 What caused the Shift in the Mean Colour between z $\sim$ 1 and z $\sim$ 0?

Figure 3.7 is discussed in sections 4.2 and 4.3 but it is immediately apparent that the mean colours of both the blue and red distributions have become redder since z $\sim$ 1. When the red and blue distributions are combined to form the total distribution, it is equally apparent that the mean colour of all galaxies has become redder with cosmic time. When considering why this has happened, there are three possibilities:

- 1) The average density of galaxies' environments has increased with cosmic time. We already know that galaxies in high density environments are redder (e.g. [21]). This can also be seen from figure 3.8.
- 2) If one looks at the evolution of galaxies at a fixed density environment, it is apparent that the fraction of red galaxies goes up with cosmic time.
- 3) Again when observing the evolution of galaxies at fixed environmental density, it is known that the mean colour of galaxies was bluer at z $\sim$ 1.

These three possibilities can be summarised by saying that the colour change of the average galaxy since z $\sim$ 1 is due to one of three parameters (or a combination of them) increasing with cosmic time. These three parameters are the average density, the fraction of galaxies that are red at constant density and the mean galactic colour (either of the red and blue distributions individually or of the combination of the two) at constant density. The third of these three possibilities amounts to saying the

galaxies are evolving in isolation. The obvious question to ask was what proportion of the colour change is due to each of the three parameters. To answer this question, I set about the following analysis.

The average colour c_{av} of all the galaxies in an epoch where f_r is the fraction of galaxies that are red and c_r and c_b are the average colours of the red and blue distributions respectively can be defined by

$$c_{av} = \frac{1}{5}\Sigma[f_r c_r + (1 - f_r)c_b] \tag{4.2}$$

where the summation is over the 5 density bins (there are equal numbers of galaxies in each of the 5 density bins) and an average over these 5 density bins has been taken. We have two epochs in which to compare the average colours: the present day (low redshift) and at $z \sim 1$ (high redshift). Using equation 4.2 with the low redshift values of densities, colours and fractions (of galaxies that are red) yields the average colour of the galaxies at low redshift. This colour is u'-r' = 2.22. The same process at high redshift gives an average high redshift colour of u'-r' = 1.49. Of the three parameters, fraction, density and colour, which is most responsible for this colour change with cosmic time? Starting with all parameters at their low redshift values, I changed them one at a time to see their relative importance.

To investigate the change due to the density, the low redshift line (the dotted line) in figure 3.8 was extrapolated (by fitting with a suitable fit and then by checking by eye) to cover the density range of the high redshift line. Then the low redshift line was interpolated to the high redshift densities and the new fractions were read off accordingly. Then these new fractions were fed into equation 4.2 to calculate the average colour the galaxies would have if only their densities took the high redshift values.

With the densities then returned to their low redshift values, I next investigated the effect of changing the fractions to the high redshift values. To do this, the high redshift line in figure 3.8 was interpolated to the low redshift density values. Then, using these low redshift densities but on the plot of fraction versus density for high redshift galaxies, the fractions were again read off, fed into equation 4.2 and the average colour the galaxies would have if only their fractions took the high redshift values was computed.

Density	Fraction	Colour (Red)	Colour (Blue)	Percentage Change
low	low	low	low	0.0
high	low	low	low	2.8
low	high	low	low	12.0
low	low	high	low	12.4
low	low	low	high	54.3
high	high	high	high	100.0

Table 4.1: The relative importance of density of environment, fraction of galaxies that are red and isolated evolution of galaxies in changing the average colour of galaxies from the z $\sim$ 1 epoch to z $\sim$ 0. The words high and low denote the high redshift and low redshift epochs whose values are assigned to each of the density, fraction and colour. For example, the third line down reveals that, when the fraction of galaxies that are red is set to the high redshift value but the density and colours of the red and blue distributions are left at the low redshift values, 12.0% of the shift in the mean colour between the epochs can be accounted for.

Finally, with all parameters returned to their low redshift values, I investigated the effect of changing the colours to their high redshift values. This was done for both the red and blue distributions together and for each distribution separately. In effect, I was measuring the change in the average colour of galaxies over cosmic time due to isolated evolution. This was done by simply changing the colours in equation 4.2 to their high redshift values.

Combinations of changing two of the three parameters were also done. For example, to investigate the effects of changing both the density and fraction to the high redshift values, the fractions were read from the high redshift line in figure 3.8 but from the points on the line that corresponded to high redshift densities. The results of this analysis are shown in table 4.1 as a percentage change in the average colour of galaxies as a result of the change in parameter values. The words "low" and "high" in the table refer to the low redshift and high redshift values of the parameters respectively.

Finally, the results displayed in table 4.1 are very powerful. They indicate very strongly that the change in the average colour of a galaxy since z $\sim$ 1 is due mostly to the

evolution of a galaxy that would occur if it were in isolation and is much less the result of any interaction between the galaxy and its environment. This is evident in the fact that only allowing the colours of the galaxies to change to their high redshift values produces 66.7% of the total change in the average colour (4^{th} and 5^{th} rows of the table combined). This is compared to just 2.8% when only the densities are allowed to take the high redshift values (2^{nd} row of the table). In fact, the change of environment causes very little change.

Chapter 5

Discussion & Conclusions

I have shown the following:

- At z $\sim$ 1, as in the local universe, the galaxies' colour distribution is bimodal
- The mean colours of the red and blue distributions change very little with density, as is the case in the local universe, although there is perhaps a faint trend of blue galaxies' colours getting redder with increasing density in the local universe.
- At z $\sim$ 1, the fraction of galaxies that are red increases with the density of the local environment. This result was also found in the local universe although the trend is stronger in the local universe.
- The average density of a galaxy's environment is slightly higher in the local universe than at high redshift.
- The density of galaxies' environments appears to play only a minimal role in the *evolution* of the mean galactic colour and, by extension, the mean galactic star formation. However, it should be remembered that, for an individual galaxy, the density can be of crucial importance.
- The vast majority of the change in mean colour is down to the natural evolution of the galaxy: stars growing old and moving off the main sequence to become red giants, gas being consumed to make new stars, gas being expelled by super winds, etc. That is, the evolution the galaxy would undertake if it were left to its own devices.

To conclude this thesis, it is worth considering what kind of galaxy formation picture is supported by the findings of this work. Firstly, the bi-modality of galaxy colours itself, both in the local universe and out to $z \sim 1$, appears to be incontrovertibly real [3, 4, 6]. This bi-modality betrays two distinct types of galaxy. Firstly, there is the "passively evolving" red population. They are passive in that star formation in these galaxies is either very low or extinct. Secondly, there is the actively star forming blue population. The bi-modality also indicates that transitions between the two populations must be relatively rapid because there cannot be a continuous spread of galaxy colours.

There is strong observational evidence for the existence of two distinct types of red galaxy that are found in clusters (for example, [34] and references therein). The first family formed their stars at high redshift ($z > 2$) over a short timescale and have been observed, mostly as luminous ellipticals, in clusters since $z\sim 1$. The second family formed their stars over a more protracted timescale and are thought only to have entered the more red, passive population as a result of interactions with other galaxies which quenched their star formation. They retain their spiral shape up to $\sim$ 1Gyr after the quenching of the star formation.

The fractions of the passive population that comprise each of the above two families will change with redshift. At higher redshift, one would expect the passive population to be dominated by the first family of "primordial" galaxies that formed in the primordial over dense regions and formed their stars quickly at high redshift. They have remained in the cluster environments ever since. As time has progressed, however, more and more of the second family, as their star formation was quenched and they had more and more time to fall into the deep potential wells of the clusters, will have joined this passive, red population.

This is certainly consistent with figure 3.8. The fraction of galaxies that are red increases with environmental density, both in the high and low redshift universes. Additionally, that trend is stronger in the local universe where, in addition to the primordial red galaxies, the second family of passive red galaxies have had time to have had their star formation quenched and to fall into the cluster centres.

Finally, a note about "downsizing" versus hierarchical models of galaxy formation. The above discussion relies upon the premise of bright galaxies already having most of

their mass in the form of stars at high redshift ($z > 1$). Ostensibly, this is contrary to the assumption of a ΛCDM hierarchical universe in which massive halos are assembled later. The fact that star formation in massive galaxies was greater at high redshift than in the local universe [50] has been taken by some as evidence for a "downsizing" model of galaxy formation. Since the ΛCDM assumption has been a central tenet of this work, it is important to resolve the apparent contradiction between ΛCDM and downsizing. [26] have recently implemented a semi-analytic model within the Millennium N-body simulation that includes feedback from Active Galactic Nuclei (AGN). This assumption is critical because the AGN are able to quench star formation in massive halos by heating the gas and quenching cooling flows. With this part of the model included, they found that the ΛCDM cosmology is consistent with the existence of a population of massive galaxies out to $z \sim 5$. The model also provides for the natural break in the luminosity function of galaxies in the local universe at bright magnitudes and predicts that star formation rate density will rise with increasing redshift in objects of all masses. Ultimately, the goal is to know how star formation evolves within the parameter space of mass, luminosity, environmental density, metallicity and redshift.

Bibliography

[1] R. G. Abraham, K. Glazebrook, P. J. McCarthy, D. Crampton, R. Murowinski, I. Jørgensen, K. Roth, I. M. Hook, S. Savaglio, H.-W. Chen, R. O. Marzke, and R. G. Carlberg. The Gemini Deep Deep Survey. I. Introduction to the Survey, Catalogs, and Composite Spectra. AJ, 127:2455–2483, May 2004.

[2] S. Arnouts, D. Schiminovich, O. Ilbert, L. Tresse, B. Milliard, M. Treyer, S. Bardelli, T. Budavari, T. K. Wyder, E. Zucca, O. Le Fèvre, D. C. Martin, G. Vettolani, C. Adami, M. Arnaboldi, T. Barlow, L. Bianchi, M. Bolzonella, D. Bottini, Y.-I. Byun, A. Cappi, S. Charlot, T. Contini, J. Donas, K. Forster, S. Foucaud, P. Franzetti, P. G. Friedman, B. Garilli, I. Gavignaud, L. Guzzo, T. M. Heckman, C. Hoopes, A. Iovino, P. Jelinsky, V. Le Brun, Y.-W. Lee, D. Maccagni, B. F. Madore, R. Malina, B. Marano, C. Marinoni, H. J. McCracken, A. Mazure, B. Meneux, R. Merighi, P. Morrissey, S. Neff, S. Paltani, R. Pellò, J. P. Picat, A. Pollo, L. Pozzetti, M. Radovich, R. M. Rich, R. Scaramella, M. Scodeggio, M. Seibert, O. Siegmund, T. Small, A. S. Szalay, B. Welsh, C. K. Xu, G. Zamorani, and A. Zanichelli. The GALEX VIMOS-VLT Deep Survey Measurement of the Evolution of the 1500 Å Luminosity Function. ApJ, 619:L43–L46, January 2005.

[3] I. K. Baldry, M. L. Balogh, R. Bower, K. Glazebrook, and R. C. Nichol. Color bimodality: Implications for galaxy evolution. In *AIP Conf. Proc. 743: The New Cosmology: Conference on Strings and Cosmology*, pages 106–119, December 2004.

[4] M. L. Balogh, I. K. Baldry, R. Nichol, C. Miller, R. Bower, and K. Glazebrook. The Bimodal Galaxy Color Distribution: Dependence on Luminosity and Environment. ApJ, 615:L101–L104, November 2004.

[5] J. E. Barnes. Formation of gas discs in merging galaxies. MNRAS, 333:481–494, July 2002.

[6] E. F. Bell, C. Wolf, K. Meisenheimer, H.-W. Rix, A. Borch, S. Dye, M. Kleinheinrich, L. Wisotzki, and D. H. McIntosh. Nearly 5000 Distant Early-Type Galaxies in COMBO-17: A Red Sequence and Its Evolution since z˜1. ApJ, 608:752–767, June 2004.

[7] M. Bernardi, R. K. Sheth, J. Annis, S. Burles, D. J. Eisenstein, D. P. Finkbeiner, D. W. Hogg, R. H. Lupton, D. J. Schlegel, M. SubbaRao, N. A. Bahcall, J. P. Blakeslee, J. Brinkmann, F. J. Castander, A. J. Connolly, I. Csabai, M. Doi, M. Fukugita, J. Frieman, T. Heckman, G. S. Hennessy, Ž. Ivezić, G. R. Knapp, D. Q. Lamb, T. McKay, J. A. Munn, R. Nichol, S. Okamura, D. P. Schneider, A. R. Thakar, and D. G. York. Early-Type Galaxies in the Sloan Digital Sky Survey. III. The Fundamental Plane. AJ, 125:1866–1881, April 2003.

[8] E. Bertin and S. Arnouts. SExtractor: Software for source extraction. A&AS, 117:393–404, June 1996.

[9] P. R. Bevington and D. K. Robinson. Data reduction and error analysis for the physical sciences. 1992.

[10] M. R. Blanton, J. Dalcanton, D. Eisenstein, J. Loveday, M. A. Strauss, M. SubbaRao, D. H. Weinberg, J. E. Anderson, J. Annis, N. A. Bahcall, M. Bernardi, J. Brinkmann, R. J. Brunner, S. Burles, L. Carey, F. J. Castander, A. J. Connolly, I. Csabai, M. Doi, D. Finkbeiner, S. Friedman, J. A. Frieman, M. Fukugita, J. E. Gunn, G. S. Hennessy, R. B. Hindsley, D. W. Hogg, T. Ichikawa, Ž. Ivezić, S. Kent, G. R. Knapp, D. Q. Lamb, R. F. Leger, D. C. Long, R. H. Lupton, T. A. McKay, A. Meiksin, A. Merelli, J. A. Munn, V. Narayanan, M. Newcomb, R. C. Nichol, S. Okamura, R. Owen, J. R. Pier, A. Pope, M. Postman, T. Quinn, C. M. Rockosi, D. J. Schlegel, D. P. Schneider, K. Shimasaku, W. A. Siegmund, S. Smee, Y. Snir, C. Stoughton, C. Stubbs, A. S. Szalay, G. P. Szokoly, A. R. Thakar, C. Tremonti, D. L. Tucker, A. Uomoto, D. Vanden Berk, M. S. Vogeley, P. Waddell, B. Yanny, N. Yasuda, and D. G. York. The Luminosity Function of Galaxies in SDSS Commissioning Data. AJ, 121:2358–2380, May 2001.

[11] R. G. Bower and M. L. Balogh. The Difference Between Clusters and Groups: A Journey from Cluster Cores to Their Outskirts and Beyond. In *Clusters of Galaxies: Probes of Cosmological Structure and Galaxy Evolution*, pages 326–+, 2004.

[12] G. Bruzual and S. Charlot. Stellar population synthesis at the resolution of 2003. MNRAS, 344:1000–1028, October 2003.

[13] K. Bundy, R. S. Ellis, and C. J. Conselice. The Mass Assembly Histories of Galaxies of Various Morphologies in the GOODS Fields. ApJ, 625:621–632, June 2005.

[14] H. Butcher and A. Oemler. The evolution of galaxies in clusters. II - The galaxy content of nearby clusters. ApJ, 226:559–565, December 1978.

[15] D. Calzetti, A. L. Kinney, and T. Storchi-Bergmann. Dust extinction of the stellar continua in starburst galaxies: The ultraviolet and optical extinction law. ApJ, 429:582–601, July 1994.

[16] S. Cole, C. G. Lacey, C. M. Baugh, and C. S. Frenk. Hierarchical galaxy formation. MNRAS, 319:168–204, November 2000.

[17] S. Cole, P. Norberg, C. M. Baugh, C. S. Frenk, J. Bland-Hawthorn, T. Bridges, R. Cannon, M. Colless, C. Collins, W. Couch, N. Cross, G. Dalton, R. De Propris, S. P. Driver, G. Efstathiou, R. S. Ellis, K. Glazebrook, C. Jackson, O. Lahav, I. Lewis, S. Lumsden, S. Maddox, D. Madgwick, J. A. Peacock, B. A. Peterson, W. Sutherland, and K. Taylor. The 2dF galaxy redshift survey: near-infrared galaxy luminosity functions. MNRAS, 326:255–273, September 2001.

[18] G. D. Coleman, C.-C. Wu, and D. W. Weedman. Colors and magnitudes predicted for high redshift galaxies. ApJS, 43:393–416, July 1980.

[19] A. W. J. Cousins. VRI Photometry of E and F Region Stars. *Monthly Notes of the Astronomical Society of South Africa*, 37:8–+, 1978.

[20] G. de Vaucouleurs. Recherches sur les Nebuleuses Extragalactiques. *Annales d'Astrophysique*, 11:247–+, January 1948.

[21] A. Dressler. Galaxy morphology in rich clusters - Implications for the formation and evolution of galaxies. ApJ, 236:351–365, March 1980.

[22] A. Dressler, A. J. Oemler, W. J. Couch, I. Smail, R. S. Ellis, A. Barger, H. Butcher, B. M. Poggianti, and R. M. Sharples. Evolution since Z = 0.5 of the Morphology-Density Relation for Clusters of Galaxies. ApJ, 490:577–+, December 1997.

[23] Wikipedia Encyclopedia. Cosmic microwave background radiation. 2005.

[24] Wikipedia Encyclopedia. Cosmic microwave background radiation. 2005.

[25] Wikipedia Encyclopedia. Wmap. 2005.

[26] Bower R. G. et al. The broken hierarchy of galaxy formation. *astro-ph/0511338*, 2005.

[27] Ciliegi P. et al. The vvds-vla deep field ii. optical and near infrared identifications of vla s(1.4ghz) gt 80 microjy sources in the vimos vlt deep survey vvds-02h field. *astro-ph/0506690*, 2005.

[28] Coil A.L. et al. The deep2 galaxy redshift survey: Clustering of groups and group galaxies at z 1. *astro-ph/0507647*, 2005.

[29] Cooper C. C. et al. Measuring galaxy environments with deep redshift surveys. *astro-ph/0511338*, 2005.

[30] Faber S. M. et al. Galaxy luminosity functions to z 1: Deep2 vs. combo-17 and implications for red galaxy formation. *astro-ph/0506044*, 2005.

[31] Hoyos C. et al. The deep2 galaxy redshift survey: Discovery of luminous, metal-poor, star-forming galaxies at redshifts 0.7. *astro-ph/0510843*, 2005.

[32] Lin L. et al. The deep2 redshift survey: Evolution of close galaxy pairs and major-merger rates up to z 1.2. *astro-ph/0411104*, 2004.

[33] Maier C. et al. Metallicities at the peak of the cosmic star formation rate: Implications for the evolution of galaxies. *astro-ph/0511255*, 2005.

[34] Poggianti B. M. et al. The evolution of the star formation activity in galaxies and its dependence on environment. *astro-ph/0512391*, 2005.

[35] Savage R.S. et al. Statistical constraints on the ir galaxy number counts and cosmic ir background from the spitzer goods survey. *astro-ph/0511359*, 2005.

[36] Willmer C.N.A. et al. The deep2 redshift survey: The galaxy luminosity function to z 1. *astro-ph/0506041*, 2005.

[37] M. Fioc and B. Rocca-Volmerange. PEGASE: a UV to NIR spectral evolution model of galaxies. Application to the calibration of bright galaxy counts. A&A, 326:950–962, October 1997.

[38] M. Fukugita, T. Ichikawa, J. E. Gunn, M. Doi, K. Shimasaku, and D. P. Schneider. The Sloan Digital Sky Survey Photometric System. AJ, 111:1748–+, April 1996.

[39] K. Glazebrook, R. G. Abraham, P. J. McCarthy, S. Savaglio, H.-W. Chen, D. Crampton, R. Murowinski, I. Jørgensen, K. Roth, I. Hook, R. O. Marzke, and R. G. Carlberg. A high abundance of massive galaxies 3-6 billion years after the Big Bang. Nature, 430:181–184, July 2004.

[40] A. W. Graham and S. P. Driver. A Concise Reference to (Projected) Sérsic $R^{1/n}$ Quantities, Including Concentration, Profile Slopes, Petrosian Indices, and Kron Magnitudes. *Publications of the Astronomical Society of Australia*, 22:118–127, 2005.

[41] J. E. Gunn and J. R. I. Gott. On the Infall of Matter Into Clusters of Galaxies and Some Effects on Their Evolution. ApJ, 176:1–+, August 1972.

[42] A. H. Guth. Inflationary universe: A possible solution to the horizon and flatness problems. Phys. Rev. D, 23:347–356, January 1981.

[43] D. Hamilton. The spectral evolution of galaxies. I - an observational approach. ApJ, 297:371–389, October 1985.

[44] A. M. Hopkins. On the Evolution of Star-forming Galaxies. ApJ, 615:209–221, November 2004.

[45] Wayne Hu. Cosmic inflation, cmb observations. 2004?

[46] Wayne Hu. Small angle anisotropies. 2004?

[47] E. Hubble and M. L. Humason. No. 427. The velocity-distance relation among extra-galactic nebulae. *Contributions from the Mount Wilson Observatory / Carnegie Institution of Washington*, 427:1–38, 1931.

[48] imamura. Hertzsprung-russell diagram. 2005.

[49] H. L. Johnson and W. W. Morgan. Fundamental stellar photometry for standards of spectral type on the revised system of the Yerkes spectral atlas. ApJ, 117:313–+, May 1953.

[50] S. Juneau, K. Glazebrook, D. Crampton, P. J. McCarthy, S. Savaglio, R. Abraham, R. G. Carlberg, H.-W. Chen, D. Le Borgne, R. O. Marzke, K. Roth, I. Jørgensen, I. Hook, and R. Murowinski. Cosmic Star Formation History and Its Dependence on Galaxy Stellar Mass. ApJ, 619:L135–L138, February 2005.

[51] R. C. Kennicutt. The integrated spectra of nearby galaxies - General properties and emission-line spectra. ApJ, 388:310–327, April 1992.

[52] R. C. Kennicutt. Star Formation in Galaxies Along the Hubble Sequence. ARA&A, 36:189–232, 1998.

[53] R. C. Kennicutt. The Global Schmidt Law in Star-forming Galaxies. ApJ, 498:541–+, May 1998.

[54] R. C. Kennicutt, D. Calzetti, F. Walter, M. K. Prescott, and SINGS Team. The Spatially-Resolved Star Formation Law in M51. *American Astronomical Society Meeting Abstracts*, 207:–+, December 2005.

[55] A. L. Kinney, D. Calzetti, R. C. Bohlin, K. McQuade, T. Storchi-Bergmann, and H. R. Schmitt. Template Ultraviolet to Near-Infrared Spectra of Star-forming Galaxies and Their Application to K-Corrections. ApJ, 467:38–+, August 1996.

[56] K Krisciunas and J Tonry. Ubvri - sloan transformations. 2002.

[57] R. G. Kron. Photometry of a complete sample of faint galaxies. ApJS, 43:305–325, June 1980.

[58] R. B. Larson, B. M. Tinsley, and C. N. Caldwell. The evolution of disk galaxies and the origin of S0 galaxies. ApJ, 237:692–707, May 1980.

[59] P. Madau. Cosmic Star Formation History. In *American Institute of Physics Conference Series*, pages 481–+, 1997.

[60] C. Marinoni, M. Davis, J. A. Newman, and A. L. Coil. Three-dimensional Identification and Reconstruction of Galaxy Systems within Flux-limited Redshift Surveys. ApJ, 580:122–143, November 2002.

[61] P. J. McCarthy, D. Le Borgne, D. Crampton, H.-W. Chen, R. G. Abraham, K. Glazebrook, S. Savaglio, R. G. Carlberg, R. O. Marzke, K. Roth, I. Jørgensen, I. Hook, R. Murowinski, and S. Juneau. Evolved Galaxies at z ¿ 1.5 from the Gemini Deep Deep Survey: The Formation Epoch of Massive Stellar Systems. ApJ, 614:L9–L12, October 2004.

[62] B. Moore, N. Katz, G. Lake, A. Dressler, and A. Oemler. Galaxy harassment and the evolution of clusters of galaxies. Nature, 379:613–616, 1996.

[63] J. B. Oke and J. E. Gunn. Secondary standard stars for absolute spectrophotometry. ApJ, 266:713–717, March 1983.

[64] A. A. Penzias and R. W. Wilson. A Measurement of Excess Antenna Temperature at 4080 Mc/s. ApJ, 142:419–421, July 1965.

[65] V. Petrosian. Surface brightness and evolution of galaxies. ApJ, 209:L1–L5, October 1976.

[66] V. Quilis, B. Moore, and R. Bower. Gone with the Wind: The Origin of S0 Galaxies in Clusters. *Science*, 288:1617–1620, June 2000.

[67] S. Savaglio, K. Glazebrook, R. G. Abraham, D. Crampton, H.-W. Chen, P. J. P. McCarthy, I. Jørgensen, K. C. Roth, I. M. Hook, R. O. Marzke, R. G. Murowinski, and R. G. Carlberg. The Gemini Deep Deep Survey. II. Metals in Star-forming Galaxies at Redshift 1.3 ¡ z ¡ 2. ApJ, 602:51–65, February 2004.

[68] J. L. Sérsic. Influence of the atmospheric and instrumental dispersion on the brightness distribution in a galaxy. *Boletin de la Asociacion Argentina de Astronomia La Plata Argentina*, 6:41–+, 1963.

[69] B. M. Tinsley. Evolution of the Stars and Gas in Galaxies. ApJ, 151:547–+, February 1968.

[70] J. L. Tonry, B. P. Schmidt, B. Barris, P. Candia, P. Challis, A. Clocchiatti, A. L. Coil, A. V. Filippenko, P. Garnavich, C. Hogan, S. T. Holland, S. Jha, R. P. Kirshner, K. Krisciunas, B. Leibundgut, W. Li, T. Matheson, M. M. Phillips, A. G. Riess, R. Schommer, R. C. Smith, J. Sollerman, J. Spyromilio, C. W. Stubbs, and N. B. Suntzeff. Cosmological Results from High-z Supernovae. ApJ, 594:1–24, September 2003.

[71] B. J. Weiner, A. C. Phillips, S. M. Faber, C. N. A. Willmer, N. P. Vogt, L. Simard, K. Gebhardt, M. Im, D. C. Koo, V. L. Sarajedini, K. L. Wu, D. A. Forbes, C. Gronwall, E. J. Groth, G. D. Illingworth, R. G. Kron, J. Rhodes, A. S. Szalay, and M. Takamiya. The DEEP Groth Strip Galaxy Redshift Survey. III. Redshift Catalog and Properties of Galaxies. ApJ, 620:595–617, February 2005.